universität wien

MASTERARBEIT / MASTER'S THESIS

Titel der Masterarbeit / Title of the Master's Thesis

„CdS dotted MOF and TiO_2 embedded electrospun PVDF-HFP fibers for photocatalytic degradation of methyl orange“

verfasst von / submitted by

Adam Elbataioui, BSc

angestrebter akademischer Grad / in partial fulfilment of the requirements for the degree of

Master of Science (MSc)

Wien, 2022 / Vienna 2022

Studienkennzahl lt. Studienblatt / degree programme code as it appears on the student record sheet:	A 066 862
Studienrichtung lt. Studienblatt / degree programme as it appears on the student record sheet:	Masterstudium Chemie
Betreut von / Supervisor:	Assoz. Prof. Jia Min Chin, PhD

Acknowledgment

I am deeply thankful for the moral support of my family during my studies and the writing of this thesis. Also, I would like to thank the whole Chin/Reithofer group for their kind help. Especially without the help of Alex who helped me with my data chaos and Robert for his support. A special supporting role in the frequent weeks play Tanja and Alex Eder for giving me a place to crash and a warm meal and also for technical feedback. Last but not least I want to state my appreciation for my supervisor Assoz. Prof. Jia Min Chin, PhD. Without her ideas, this project would not be possible.

Zusammenfassung

Ziel dieser Masterarbeit war es, eine photoaktive Verbindung in ein Polymer mit piezoelektrischen Eigenschaften einzubetten, um die Ladungstrennung zu verbessern und damit die Langlebigkeit der erzeugten Ladungen zu verlängern. Als Vertreter organischer Schadstoffe wurde der Azofarbstoff Methylorange (MO) als Proof-of-Concept-Komponente ausgewählt. MO wurde als Vertreter der Familie der Azofarbstoffe ausgewählt, die für ihre hohe Persistenz in der Umwelt bekannt sind.[1] Der photokatalytische Abbau von Azofarbstoffen mit TiO_2 ist bereits breit untersucht worden sowohl alleinstehend als auch in Kombination mit anderen Substanzen.[2] Die hier vorliegende Arbeit baut auf diesem Wissen auf, um ein kostengünstiges wiederverwendbares Verbundmaterial welches auch eine lange Zeit haltbar ist für den photokatalytischen Abbau von MO herzustellen. Als elektrogesponnene Faser weist Poly-(vinylidenfluorid-co-hexafluorpropylen) (PVDF-HFP) Piezoelektrizität auf, die bei mechanischer Verformung die Ladungstrennung der durch ultraviolettes Licht (UV) aktivierten Komponenten unterstützt. Das erzeugte Potenzial innerhalb des Verbundstoffs erleichtert die Erzeugung von Ladungen. In zwei Ansätzen wurden zwei verschiedene UV-aktive Materialien in die Fasern integriert. Einerseits wurde TiO_2 über den Vorläufer $Ti(iOPr)_4$ in die Polymerlösung implementiert und anschließend hydrolysiert. Zum anderen wurde eine Polymerlösung mit der metallorganischen Gerüststruktur (MOF) UiO-66-NH_2 mit integrierten CdS-Quantumdots in die Fasern eingebettet. Um den Abbau von Methylorange zu verfolgen, wurde 1-Methyl-Imidazol als interner Standard gewählt. Die neuen Kompositfasern wurden mittels Sekundärelektronenmikroskopie (SEM), Pulverröntgendiffraktometrie (PXRD) und Kontaktwinkelmessungen (CA) charakterisiert. Es wurde ein erhöhter Anteil der β-Phase PVDF-HFP erreicht, die in der Zusammensetzung vorherrschte und mittels PXRD und Infrarotspektroskopie (IR) als piezoelektrische Kristallphase nachgewiesen wurde. Die Integration von TiO_2 in eines elektrogesponnenen Verbundmaterials wurde erreicht. Dies konnte durch Kontaktwinkel (CA) Messungen bestätigt werden. Die MOFs UiO-66 und UiO-66-NH_2 als auch die Qantumdot intergireten MOFs UiO-66@Cds und UiO-66-NH_2@CdS wurden hergestellt. Die Porosität der MOF-Struktur UiO-66-NH_2 mit integrierten CdS-Quantumdots wurde mit der Brunauer-Emmet-Teller-Methode (BET) untersucht und zeigte nanoporöse Strukturen und der photokatalytische Effekt auf den pH-Wert ist beobachtet worden. Die Degradation von MO und die Konzentration des internen Standards wurden mittels UV/Vis-Spektroskopie verfolgt und bestätigten die Abnahme der Farbstoffkonzentration. In diesem Projekt wurde ein erfolgreiches Verfahren für geeignete Faserverbundwerkstoffe und ein verbessertes β Phasenver-

hältnis entwickelt und die Fasern wurden vollständig charakterisiert. Der MO-Abbau mit $Ti(iOPr)_4$-Fasern wurde erreicht und mittels Ultraviolett-Spektroskopie (UV/vis) verfolgt. Die Synthese von TiO_2-Kristallen auf der Faseroberfläche wurde durchgeführt und vollständig analysiert.

Abstract

The aim of this master thesis was to embed a photoactive compound into a polymer with piezoelectric properties to enhance the separation of photogenerated charges and therefore prolong their longevity. To evaluate the ability to degrade pollutants the azo dye methyl orange (MO) was selected as a proof-of-concept component. MO was chosen as a representative of the azo dye family which is known for their high persistence in the environment.[1] The photocatalytic degradation of azo dyes with TiO_2 is already broadly investigated by itself and also in combination with different compounds.[2] As an electrospun fiber poly-(vinylidenfluoride-co-hexafluoropropylene) (PVDF-HFP) shows piezoelectricity which aids in the charge separation of the ultra violet (UV) activated components during mechanical deformation. The generated potential within the composite facilitates the charge separation via UV radiation. Solutions of $Ti(iOPr)_4$ and PVDF-HFP mixtures were electrospun and the resulting fibermat was incubated. To generate MOF/PVDF-HFP fibers the MOF and MOF@CdS were first synthesised and then mixed with PVDF-HFP polymer solution to obtain the fibermat. The fibers were tested for photocatalytic activity under UV-light. Synthesied MOF and MOF@CdS were analysed on their photocatalytic potential. To follow the degradation of methyl orange, 1-methyl-imidazole was selected as an internal standard. The new composite fibers were characterized via Scanning Electron Microscopy (SEM), Powder X-Ray Diffraction (PXRD), and contact angle measurements (CA). Enhancement of the β phase as the piezoelectric crystal phase of PVDF-HFP was achieved and predominated the composition which was shown in PXRD and Infrared Spectroscopy (IR). Fabrication of fibers containing TiO_2 could be confirmed via contact angle (CA) measurement. The MOFs UiO-66 and UiO-66-NH_2 as well as the nanocomposites UiO-66@Cds and UiO-66-NH_2@CdS have been produced. The porosity of the MOF structure UiO-66-NH_2 with integrated CdS quantum dots was investigated with the Brunauer-Emmet-Teller method (BET) which showed nanoporous structures and a photocatalytic effect on the pH was observed. Degradation of MO and the concentration of internal standard were followed via UV/Vis spectroscopy and confirmed the decrease in the concentration of the dye. In this project, a successful procedure for fiber composites and enhanced β phase ratio was established. Those fibers were fully characterised and further tested for their photocatalytic activity. Synthesis of TiO_2 crystals on the fiber surface was accomplished and fully analysed.

Contents

1 Theoretical part **12**

1.1 Electrospinning . . . 12

1.1.1 Principle of electrospinning . . . 12

1.2 PVDF and piezoelectricity . . . 14

1.3 MOFs . . . 16

1.3.1 MOF@QD . . . 16

1.4 TiO_2 . . . 17

1.4.1 UV activation . . . 18

1.4.2 Fluorescence spectroscopy . . . 18

1.4.3 Hydrophobic surfaces . . . 19

1.5 Contamination of water with organic compounds . . . 19

1.5.1 Azo dyes . . . 20

2 Experimental Part **21**

2.1 Synthesis of MOF and CdS . . . 21

2.1.1 UiO-66 . . . 21

2.1.2 UiO-66-NH_2 . . . 21

2.1.3 CdS . . . 21

2.1.4 Synthesis of UiO-66-NH_2@CdS . . . 21

2.1.5 Synthesis of UiO-66@CdS . . . 22

2.2 Fabrication of fiber . . . 22

2.2.1 Fabrication of UiO-66-NH_2-PVDF-HFP polymer solution . . . 22

2.2.2 Fabrication of TiO_2 fiber . . . 23

2.2.3 Fabrication of Ti(iOPr)$_4$-PVDF-HFP fiber . . . 23

2.2.4 Fabrication of Ti(iOPr)$_4$-PVDF-HFP fiber with GNT and GO . . . 24

2.3 Growth of TiO_2 crystals on the fibers . . . 24

2.4 Catalysis . . . 24

2.5 UV spectroscopy . . . 27

2.6 pH measurement . . . 27

2.6.1 Catalysis with TiO_2 powder . . . 27

2.7 Contact angle measurement . . . 27

3 Results and discussion **29**

3.1 Synthesis of MOF and CdS 29

3.1.1 BET measurements of MOFs 31

3.1.2 TEM images of UiO-66-NH_2 and UiO-66-NH_2@CdS 31

3.1.3 Fabrication of UiO-66-NH_2-PVDF-HFP fiber 32

3.1.4 CdS QDs 33

3.1.5 Fluorescence spectroscopy 33

3.1.6 Catalysis with TiO_2 powder 34

3.1.7 pH measurement 35

3.2 Fibermat synthesis 38

3.2.1 Fabrication of TiO_2 fiber 38

3.3 Growth of TiO_2 crystals on electrospun fibers 38

3.4 Contact angle measurements 40

3.4.1 TEM of Fibers with $Ti(iOPr)_4$ 41

3.5 Crystal phases of PVDF-HFP 42

3.6 Catalysis with fibermat 43

3.6.1 Catalysis with $Ti(iOPr)_4$-PVDF-HFP fibermat 44

3.6.2 Catalysis with $Ti(iOPr)_4$-PVDF-HFP-GNT fibermat 45

3.6.3 Catalysis with $Ti(iOPr)_4$-PVDF-HFP-GO fibermat 46

3.6.4 Comparison of fibermat catalysis 47

4 Conclusion and outlook **48**

List of abbreviations

ATR-FTIR	Attenuated total reflection fourier-transform infrared spectroscopy
BET	Brunauer-Emmet-Teller method
CA	Contact angle
DMF	Dimethylformamide
EDX	Energy dispersive X-ray spectroscopy
GNT	Graphene nanotubes
GO	Graphene oxide
IR	Infrared
MO	Methyl orange
MOFs	Metal-organic frameworks
PXRD	Powder X-ray diffraction
SEM	Scanning electron microscope
TEM	Transmission electron microscope
TAA	Thioacetamide
TCD	Tip-to-collector distance
TGA	Thermogravimetric analysis
UV	Ultraviolet
Vis	Visible light

1 Theoretical part

1.1 Electrospinning

The principles of electrospinning were discovered in 1887 by Charles V. Boys when it was shown that fibers could be obtained from a viscoelastic liquid in an external electric field.[3] Upon this discovery it was possible for the first time to artificially achieve ultra thin fibers apart from natural phenomena as in spiderwebs or silkworms.[4][5] Fibers as the cornerstone of fabric production are an essential starting point for further applications in real-world scenarios.[6] The first commercially available fiber Nylon by the company DuPont established in 1938 was of high interest due to the wide variety of different polyesters and their performance as fibers.[7] Those polyesters differ in the length of the aliphatic chains as well as in their molecular weight which affects their behaviour while electrospinning. The possibility to introduce aromatic rings as seen in poly(ethylene terephthalate) broadens the range of applications.[8] The research in new fibers has been important in the new development in the textile industry and found its way in the lives of many. The first patents of an electrospinning setup were reported in 1902 by John Cooley and William Morton at the same time.[9][10] One of the most popular applications of electrospun nanofibers is air filtration due to the high surface-to-volume ratio.[11] Since then the field of electrospinning has been developed and has seen especially in the last two decades rapid growth.

1.1.1 Principle of electrospinning

As a reliable method for generating ultra-thin fibers, electrospinning has been established as a versatile technique. It is an electrohydrodynamic process in which a droplet is charged via a high-voltage field. The applied voltage between the needle and the grounded collector charges the polymer solution which flows through that needle. Thus, a jet is generated which is elongated to form fibers while the solvent evaporates.[12]

The device consists of only a high-voltage power supply, a pressure conveyed polymer solution feeding system, a conducting needle and a grounded collector. Due to its rather simple set-up and device requirements an electrospinner may be operated in every laboratory.[13]

The whole process can be separated in five different stages: formation of the Taylor Cone, stretching of a charged jet, thinning of the jet, solidification and the deposition of the fibers.

The potential difference between the needle and the collector ensures the separation of positive and negative charges in the solution by an external high voltage electric field. The charges which

migrate to the surface disturb the surface tension, resulting in a distorted shape which is the Taylor cone. Important to notice is that the more viscous the polymer solution is a higher voltage is needed to disturb the surface tension.[14]

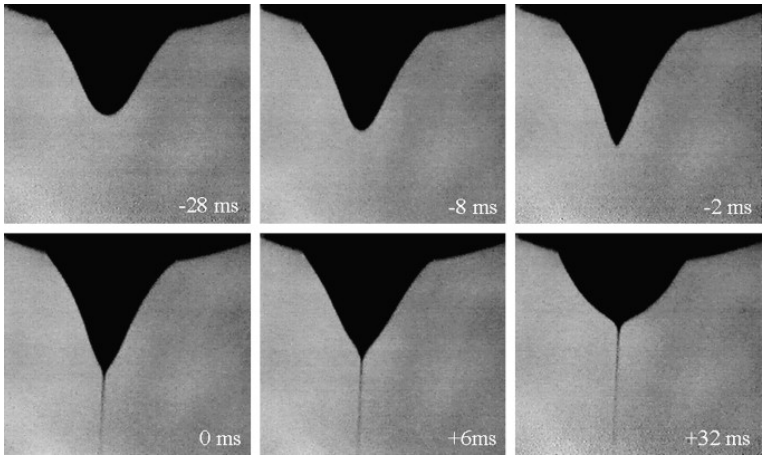


Figure 1: Stages of the jet[15]

The shape of the droplet of the polymer solution is shown in the figure above in 6 images taken from a video. The time mark 0 ms indicates the formation of the so-called Taylor cone in an electric field. The potential was applied at -28 ms and the change of shape was observed. One sees that the droplet is elongated to a conical shape before ejecting the jet. That shape can be sustained as long as the liquid can be provided. If the electric field is too strong to maintain the shape of the Taylor cone, the jet gets disconnected. [15]

The Taylor cone needs to be supplied by an adequate amount of polymer solution to maintain its shape.[16]

A jet is then ejected from the tip of the Taylor cone and accelerated when the critical amount of charge is observed.[17] Stretching and thinning occurs when the jet is accelerated due to the instability of the coil which causes whipping. Those inturbations are a product of the interaction between the charges in the jet and the external electric field.[12] The solvent then evaporates and results in a solid polymer fiber which can be collected on the grounded collector plate.[17]

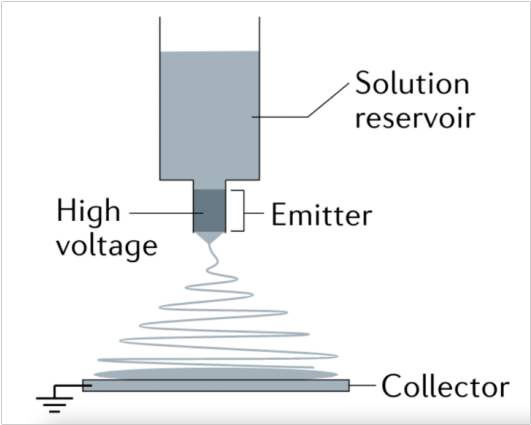


Figure 2: schematic setup of electrospinning [18]

1.2 PVDF and piezoelectricity

Piezoelectricity is the effect of producing an electric field by applying a force on certain crystals. That effect is originated in the constellation of the crystal and its contained charges. The potential from that physical deformation is converted into an electric potential through the material.[19] The charges in a crystal serve as a capacitor. A capacitor uses the fact of spatial separated charges which are given in the piezoelectric crystal. If the charges move to each other or apart from each other the potential changes.[20]

$$C = \varepsilon A/d \tag{1}$$

C: capacity; ε: permittivity; A: area; d: distance between charged surfaces

The permittivity ε is a a measure of electric polarisability in materials and is specific for each dielectric compound. The capacity is rising with a larger the area of the capacitor and falling with larger distances of the opposing charges. The mechanical proprieties of the polymer can be determined by its crystal phases. PVDF-HFP in its β phase shows piezoelectricity.[20] Therefore it is of high interest to regulate the composition to achieve the desired effect. The three most common crystalline phases of PVDF are α, β and β. The alpha phase appears most common by melting the polymer and letting it cool at ambient conditions.

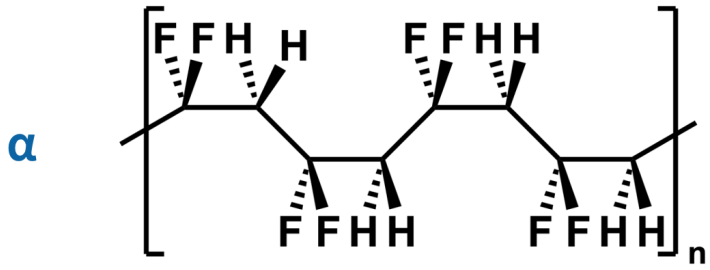


Figure 3: Alpha phase of PVDF

As seen in Fig. 3 the α phase has no overall dipole. That is due to the carbon chain arrangement in which the fluorine substituents and the hydrogen substituents point in the same direction resulting in a partial positive and partial negative charge also pointing in the same direction and giving a net zero charge. Fluorine, as the most electronegative element in the periodic table has a negative partial charge while bonding to a carbon and hydrogen has a positive partial charge while bonding with carbon.

The beta phase which is a polar phase and the desired one due to fact that it shows piezoelectricity.

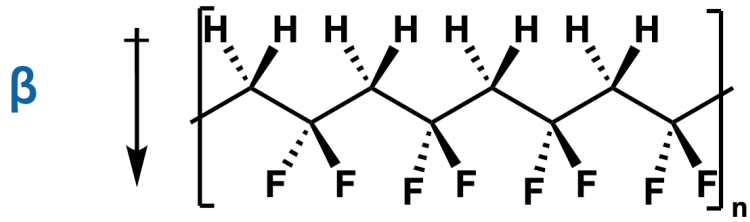


Figure 4: Beta phase of PVDF

It was shown that the beta phase can be achieved with electrospinning. By applying an external high voltage field the dipole of the polymer molecular level are forced to align with the electric field and results in an arrangement of sheets of dipols. Each layer is a molecular capacitor and have collectively a measurable effect which can be exploited.[21]

And the gamma phase which is also polar but has no piezoelectric proprieties.[22]

Although the Hexafluorpropylene group is substituted the crystalline phases can be applied and the piezoelectric effect can be observed and exploited.

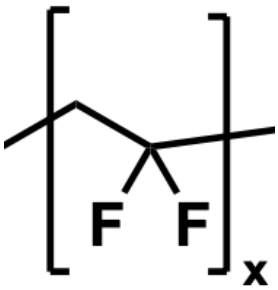


Figure 5: PVDF

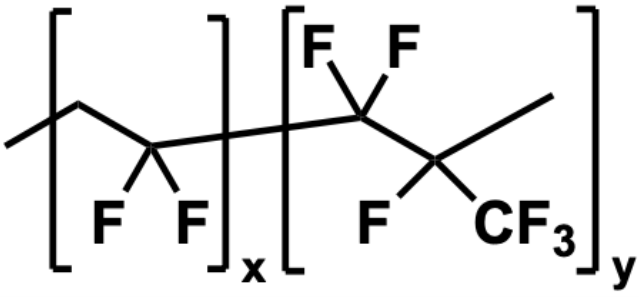


Figure 6: PVDF-HFP

1.3 MOFs

Metal organic Frameworks (MOFs) are a porous compound class consisting of metal ions and organic linkers which have a bridging trait resulting in a crystalline structure which expands in two or three dimensions.[23] They are defined by their polymeric nature residing in an area between coordination chemistry and material science.[24] The pore sizes and surface area of MOFs can be managed through the unique merging of inorganic and organic molecular building blocks. The strong ionic bonding between the metal and the linker allows for an extended structure which results in a high ordered crystalline phase.[25][26] The structure of MOFs show anisotropy, which is a characteristic of some crystals where the structure does not show the same periodic repeating units in all three dimensions. That opens up hollow channels in one dimension in MOFs which than be exploited.[27]

1.3.1 MOF@QD

Nanoparticles are commonly classified as particles ranging from the size of 1-100 nm in at least one dimension. Particles which are made from semiconducting materials and showcase quantum mechanical proprieties are called Quantum dots. This emerges at sizes smaller than 10 nm.[28] That results in a small bandgap and photo-pysical properities wich are determined by the size of the particles.[29]

Linkage of QDs and MOF have been already reported for catalytic processes. Through that linkage a narrowing of the wide bandgap from the MOF is achieved and the excitation energy barrier is reduced.[30]

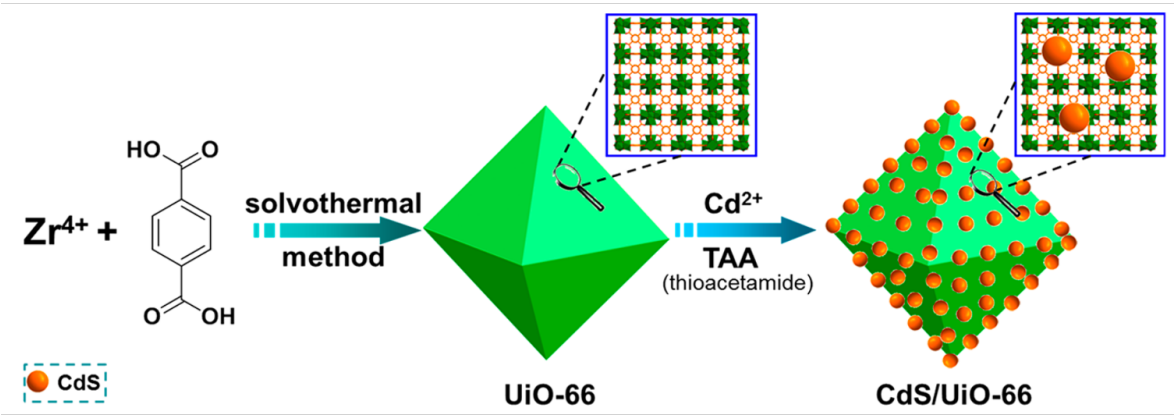


Figure 7: Schematic overview of the preparation of UiO-66@CdS [30]

Figure 8 shows a schematic overview of the general synthesis of UiO-66@CdS. In A solvothermal reaction the octahedral MOF is synthesised with its highly porous surface area. In a next step the CdS QDs are deposited in those pores to achieved the CdS dotted MOF.

Photochemical reactions with MOFs have been a field of interest due to the high variety of possible metal ions and organic linkers.[31] The charge separated states created by photo-excitation can migrate over a long distance at MOF/solvent interfaces directly over the solvent molecules or via electron transfer reactions. Channeling of MOFs play a huge role in the aid of that effect.[31]

1.4 TiO_2

TiO_2 as a non toxic cheap chemical is broadly used in different aspects of the daily life such as in white paint and chewing gum.[32][33] TiO_2 has three crystalline phases: anatase, rutile and brookite whereas the thermodynamically most stable one is rutile and the most common available ones are anatase and rutile. [34] Anatase shows photocatalytic activity in UV light and degradation of various pollutants. [35]

Due to to the low cost, high efficiency and non toxicity TiO_2 is one of the cheapest semi-conducting metal oxide photocatalyst with a broad area of application. [36]

Anatase is more active than rutile for different reasons. It has compared to rutile a higher surface area making it more attractive for heterogeneous catalysis. Furthermore the bandgap is slightly higher resulting in a larger redox capacity. Lastly an enhanced charge separation is given due to more oxygen vacancies. [37]

1.4.1 UV activation

UV light with the wavelength of 365 nm holds the energy necessary to excite electrons in TiO_2 which then become available for further chemical reactions like bond breaking and others. [38]

$$TiO_2 + h\nu \rightarrow e^- (TiO_2\text{-CB}) + h^+ (TiO_2\text{-VB})$$

Figure 8: Reaction scheme of UV activation of TiO_2 to conducting band (CB) and valence band (VB)

The excitation of an electron on the surface of any material via light is categorised as a photochemical reaction. In this case the light with a wavelength of 365 nm provides the necessary energy to provoke a charge separation by exciting an electron from its ground state into its excited state. Resulting in a TiO_2 crystal with an empty conducting band (CB) and an occupied valence band (VB). Three possible outcomes of the electrons and holes can be determined: the first one is the recombination of them in bulk or the surface and releasing the energy from the photons; the second is the electron and the hole migrating to the surface and then to the solvent or reactant; the third and last one is that they are trapped by defects in the structure. The second process is the one where a photocatalytic reaction takes place in which the electrons and holes can react with the substrate. [39]

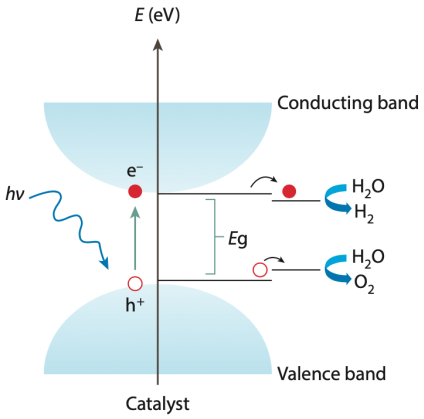


Figure 9: [38]

1.4.2 Fluorescence spectroscopy

The general aim is to define a wavelength range to excite the sample and then to measure in an 90° angle the emitted wavelength. If the sample is fluorescent, the resulting wavelength is typically observed at a greater wavelength and a sharp signal.[40]

As the excited state is partly stabilised it shows a $\triangle$E to the ground state which is not dependent of the excitation-wavelength. The magnitude of the Stokes shift and the wavelength is a result of the interaction (polar, static hydrogen bonding) of the molecule in the given solvent.[41]

$$E = h\nu \tag{2}$$

The Planck relation explains the context of the energy of a system to the wavelength.[42]

1.4.3 Hydrophobic surfaces

To determine the interaction between a liquid and a solid surface the contact angle (CA) can be a means of measure. The CA is determined by the angle a single droplet of the liquid has to the surface. If the CA of water is below 90° the surface is considered hydrophilic, if it is above 90° it is considered hydrophobic. If the CA of a water droplet exceeds 150° then the surface is considered to be superhydrophobic. Not only the material of the surface influences the CA but also the roughness.[43]
Modifying the surface by for example adding silanes can open up new possibilities for self cleaning superhydrophobic surfaces which can imitate behaviour seen previously in nature as in lotus leaves.[44]

1.5 Contamination of water with organic compounds

Of the total water covering the earth 97% is saltwater. Only 0.5% of the global water is reserved as natural freshwater and therefore can be used for human consumption.[45] Water as the most important commodity is necessary for human life. Around 40% of the human population has no or limited access to clean water, therefore it is imperative to assure access to clean water for the population.[46] Groundwater contributes to around 95% of fresh water but is at risk from the growing agriculture and its pesticide use.[47] To assure the provision of drinking water for the growing population new methods of the safe reuse of contaminated water have to be developed. Industrial and agricultural water waste treatment has been using biological processes for the removal of organic pollutants. That is achieved by the means of enzymes or bacteria which does not allow for a complete degradation for non biologically decomposing pollutants.[48] To remove pollutants completely a combination of physical and chemical processes can be applied which can be more costly than others but operate faster.[49]

1.5.1 Azo dyes

Azo dyes show a characteristic azo group (-N=N-) and aliphatic substituents which allows for a de-located π system. This chemical stability allows for a wide range of use but is also harmful to the environment. [50]

Azo dyes have been shown to have a carcinogenic effect on humans and an overall bad health influence when ingested. [51]

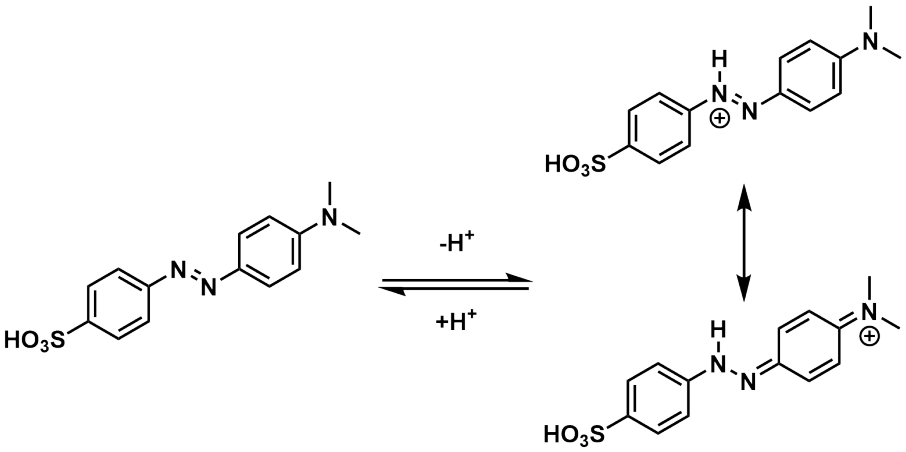


Figure 10: pH indication activity of MO

MO shows a protonation at pH 3.1-4.4 and hence a shift in colour because the electronic system is affected. [52]

2 Experimental Part

2.1 Synthesis of MOF and CdS

2.1.1 UiO-66

According to literature $ZrCl_4$ (0.2332 g, 1.0 mmol, 1 eq.) and terephthalic acid (0.1812 g, 1.0 mmol, 1 eq.) were dissolved in DMF (50 mL), afterwards the solution was transferred to a 90 mL Teflon-lined stainless steel autoclave. The autoclave was sealed and heated in an oven at 120 °C for 48 h. The resulting dispersion was filtered via fritted glass and washed several times with anhydrous methanol. The obtained white crystals were dried under vacuum at 60 °C for 24 h.[53]

2.1.2 UiO-66-NH_2

According to literature $ZrCl_4$ (0.2326 g, 1.0 mmol, 1 eq.) and 2-NH_2-benzenedicarboxylate (0.1793 g, 1.0 mmol, 1 eq.) were dissolved in DMF (50 mL), afterwards the solution was transferred to a 90 mL Teflon-lined stainless steel autoclave. The autoclave was sealed and heated in an oven at 120 °C for 48 h. The resulting dispersion was filtered with a fritted glass and washed several times with anhydrous methanol. The obtained white crystals were dried under vacuum at 60 °C for 24 h.[54]

2.1.3 CdS

According to literature In 30 mL DMSO $Cd(CH_3COO)_2$ x 2 H_2O (0.106 g, 0.398 mmol) was dissolved and stirred vigorously. The solution was poured into a Teflon-lined stainless steel autoklave (60 mL) and heated at 180 °C for 12 h. After cooling to room temperature, the yellow solid was collected and then washed via centrifugation with water (2x20 mL) and ethanol (2x20 mL) at 7000 rpm for 8 min. The product was dried at 60 °C under vacuum for 12 h.[55]

2.1.4 Synthesis of UiO-66-NH_2@CdS

According to literature $Cd(CH_3COO)_2$ x 2 H_2O (8.1 mg, 0.03 mmol, 1 eq.) was dissolved in 10 mL ethanol. Then UiO-66 (40 mg) was mixed with the solution and then sonicated for 30 min. The suspension was heated at 80 °C for 10 min, to which 10 mL of aqueous solution of TAA (2.3 mg, 0.03 mmol, 1 eq.) was added into the flask dropwise at 80 °C for a period of 30 min and stirred vigorously. The reaction mixture was stirred for another 30 min. The precipitate was washed via centrifugation with water (2x20 mL) and ethanol (2x20 mL) at 7000 rpm for 8 min. The product was

dried at 60 °C under vacuum for 12 h.[30]

2.1.5 Synthesis of UiO-66@CdS

Procedure as adapted from literature: $Cd(CH3COO)_2$ x 2 H_2O (8.1 mg, 0.03 mmol, 1 eq.) were dissolved in 10 mL ethanol. Then UiO-66 (40 mg) was added to the solution and then sonicated for 30 min. The suspension was heated at 80 °C for 10 min, to which 10 mL of aqueous solution of TAA (2.3 mg, 0.03 mmol, 1 eq.) was added into the flask dropwise at 80 °C for a period of 30 min and stirred vigorously. Then, the suspension was heated at 80 °C and stirred for another 30 min. The precipitate was washed via centrifugation with water (2x20 mL) and ethanol (2x20 mL) at 7000 rpm for 8 min. The product was dried at 60 °C under vacuum for 12 h.[30]

2.2 Fabrication of fiber

Preparation of the stock solution: The polymer was prepared in a stock solution by dissolving PVDF-HFP in DMF overnight at 40 °C, then stirred in an overhead stirrer for 5 min at 1000 rpm and degassed in an desiccator under reduced pressure.

A teflon tube connected to the needle was pre-filled with the polymer solution on applying vacuum at the needle-tip. Parameters as the Argon pressure and the applied Voltage were adjusted manually to achieve fibers. The exact conditions are listed in tables 1-3 for each sample. After a stable Taylor cone is established the desired collector surface was installed and the fibers were deposited onto it. PVDF-HFP with a molecular weight of 400.000 g/mol as polymer pellets were chosen because the viscoelasticity of the solution allows for a facile processing while ensuring the ability for a smooth electrospinning process. PVDF-HFP also exhibits less brittle and a more elastic behaviour then PVDF after electrospinning making it the more desirable choice for further processing.[56]

2.2.1 Fabrication of UiO-66-NH_2-PVDF-HFP polymer solution

10 wt% of MOF according to PVDF-HFP weight were sonicated in DMF for 10 min. The dispersion was heated at 40 °C and stirred with a stirring bar while the polymer pellets were added and the mixture stirred overnight. The desired amount of polymer solution was removed for the preparation of the composite in a next step.

The following table shows the electrospinning parameters.

Table 1: Parameters for electrospinning

Sample	**Material**	**Voltage** (kV)	**Pressure** (kPa)	**Humidity** (%)	**Temp.** (°C)
ADEL 13	PVDF-HFP + UiO-66	10.11	70.0	12.1	24.5

2.2.2 Fabrication of TiO_2 fiber

The polymer stock-solution was prepared using DMF as a solvent and 25 wt% PVDF-HFP. An amount of TiO_2 equal to 20% of the net weight of PVDF-HFP was stirred into the solution with an overhead stirrer. This yielded the final solution which was immediately processed further for electrospinning.

The following table shows the electrospinning parameters.

Table 2: Parameters for electrospinning

Sample	**Material**	**Voltage** (kV)	**Pressure** (kPa)	**Humidity** (%)	**Temp.** (°C)
ADEL 24	PVDF-HFP + TiO_2	5.96	30.0	24.1	23.9
ADEL 32	PVDF-HFP + TiO_2	5.2	70.0	28.6	22.8

2.2.3 Fabrication of $Ti(iOPr)_4$-PVDF-HFP fiber

The polymer stock-solution was prepared using DMF as a solvent and 25 wt% PVDF-HFP. An amount of $Ti(iOPr)_4$ equal to 20% of the net weight of PVDF-HFP was stirred into the solution with an overhead stirrer. This yielded the final solution which was immediately processed further for electrospinning.

The following table shows the electrospinning parameters.

Table 3: Parameters for electrospinning

Sample	**Material**	**Voltage** (kV)	**Pressure** (kPa)	**Humidity** (%)	**Temp.** (°C)
ADEL 24	PVDF-HFP	6.98	30.0	20.7	23.3
ADEL 29	PVDF-HFP + $Ti(iOPr)_4$	9.05	40.0	2.4	25.0
ADEL 31	PVDF-HFP + $Ti(iOPr)_4$	10.17	40.0	0.2	27.3

2.2.4 Fabrication of Ti(iOPr)$_4$-PVDF-HFP fiber with GNT and GO

For fibers containing graphene nanotubes (GNT) and graphene oxide (GO) 2 wt% were added to the DMF, sonicated for 5 min and then the PVDF-HFP (20 wt%) was added under magnetic stirring overnight at 40 °C. After that 20% of the net weight from the PVDF-HFP Ti(iOPr)$_4$ was given into the solution under argon atmosphere to inhibit hydrolysis and stirred to obtain the final solution which was immediately processed further.

The following table shows the electrospinning parameters.

Table 4: Parameters for electrospinning

Sample	**Material**	**Voltage** (kV)	**Pressure** (kPa)	**Humidity** (%)	**Temp.** (°C)
ADEL 37	PVDF-HFP + GNT + Ti(iOPr)$_4$	10.94	70.0	48.2	23.7
ADEL 38	PVDF-HFP + GO + Ti(iOPr)$_4$	10.39	70.0	42.7	24.1

2.3 Growth of TiO_2 crystals on the fibers

Procedure for growth of TiO_2 crystals on the fibers was adapted from literature:

The already electrospun fibermat ADEL 29 was fixed on glass-slides and used for hydrothermal reaction. An aqueous solution of urea (0.5 M, 60 mL, eq.) and Ti(iOPr)$_4$ (0.125 M, 2.05 mL, eq.) was stirred vigorously and then transferred with three glass-slides into a teflon lined stainless steel autoclave (90 mL) and heated for 24 h at 120 °C. The glass-slides were then removed, washed with milli-Q water and air dried for 24 h on air.[57]

2.4 Catalysis

General procedure:

Catalysis was performed in milli-Q water (500 mL), 1-Methylimidazole (2.54x10^{-4} mol/L), 1.5 μL) as internal standard and MO (2x10^{-5} mol/L). Three PVDF-HFP composite coated glass-slides were placed each on one silicone wedge of the dimensions 5.4 cm x 4 cm and an inclination of 36°.

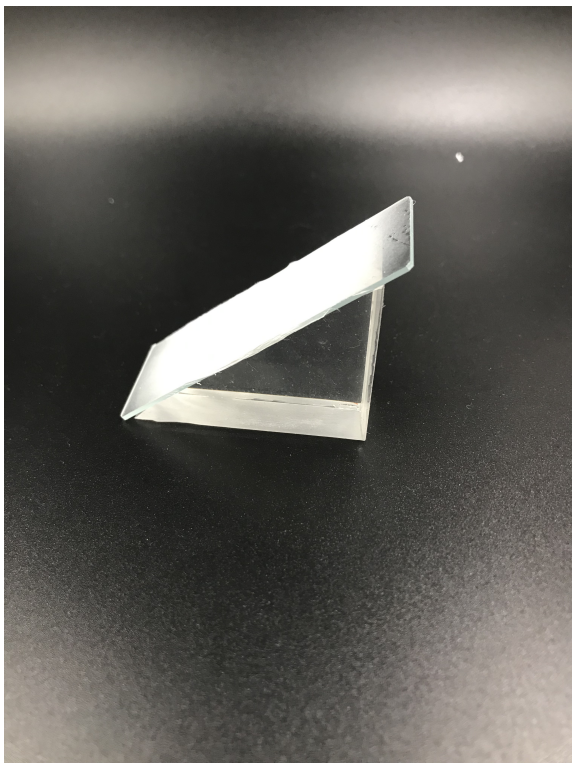


Figure 11: Glass-slide deposited fibermat on silicone wedge for photocatalysis

The solution was stirred in the dark for 40 min to establish equilibrium. 1 mL of solution was extracted every 30 min for a period up to 210 min and stored in the dark for analysis in the UV spectrometer.

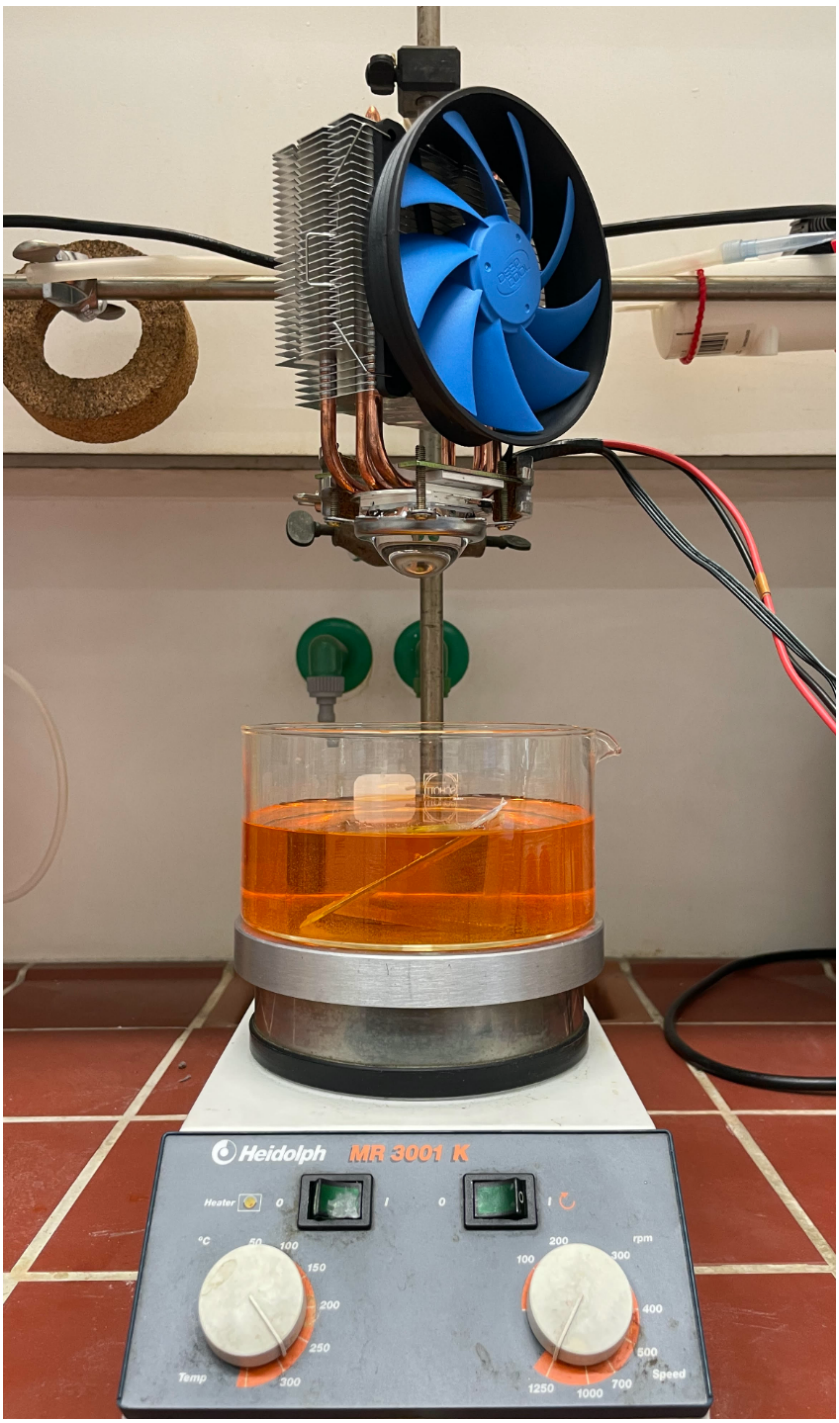


Figure 12: Set up for photocatalytic degradation

This figure shows the setup which was used for photocatalytic degradation of MO. A wide beaker was placed on a magnetic stirrer and the UV lamp was fixed above it. Three glass-slides were placed on silicone wedges in 500 mL of MO solution. A magnetic stirring bar was added and the solution was stirred at 300 rpm.

2.5 UV spectroscopy

For the measurement of the UV absorbance spectra a quartz cuvette with a width of 10 mm with a maximum volume of 1.4 mL was used. The spectra were measured from 190 nm to 1100 nm. The peak position and the peak-height was identified. A blank measurement was recorded from milli-Q water was taken before each series of samples.

2.6 pH measurement

The substrate listed in table 5 was dispersed in a beaker with milli-Q water (200 mL) and stirred vigorously. pH was measured at ambient conditions and the value was taken at specific time intervals. The UV lamp was switched on at 0 minutes and switched off at 90 minutes to determine if the pH recovers. Approximately 40 mg of substrate was added to 200 mL milli-Q water and stirred with a magnetic stirring bar.
The following table shows the exact weight of the substrate used for the photocatalytic pH experiment.

Table 5: Exact weight of the substrate

UiO-66	**UiO-66-NH_2**	**UiO-66@CdS**	**UiO-66-NH_2@CdS**
38.98 mg	39.60 mg	38.74 mg	39.72 mg

2.6.1 Catalysis with TiO_2 powder

In a wide beaker milli-Q water (500 mL), TiO_2 (81.91 mg, 38 eq.) and MO (2.15 mg, 1 eq.) were added at once and stirred in the dark for 40 min. The subsequent measurements were performed according to the mentioned procedure.

2.7 Contact angle measurement

CAs of the following fibermats were measured with milli-Q water. The glass-slides covered with the fibers were placed in the device and a drop was placed as near as possible to the edge to ensure a better quality of measurements.
CAs of ADEL 24/29/31/32/37/38 were measured.
The following table shows the composition of the fabricated fiber mats.

Table 6: Composition of the fabricated fiber mats

Sample	**Material**
ADEL 24	PVDF-HFP + TiO_2
ADEL 29	PVDF-HFP + $Ti(iOPr)_4$
ADEL 31	PVDF-HFP + $Ti(iOPr)_4$ after 2 weeks incubation
ADEL 32	PVDF-HFP + TiO_2 after 2 weeks incubation
ADEL 37	PVDF-HFP + $Ti(iOPr)_4$+ GNT
ADEL 38	PVDF-HFP + $Ti(iOPr)_4$ + GO

3 Results and discussion

3.1 Synthesis of MOF and CdS

When comparing the PXRD spectra of the MOFs UiO-66 and UiO-66-NH_2 with the respective literature a successful synthesis can be confirmed.[54] The dominant peaks at 2θ = 7.3, 8.6 and 25.6° can be observed in UiO-66 as well in UiO-66@CdS.[58] The dominant peaks at 2θ = 7.4, 8.6 and 25.8° can be observed in UiO-66-NH_2 as well as in UiO-66-NH_2@CdS.[59]

The diffraction pattern of CdS is in accordance to the literature [55] and can be observed in UiO-66 as well as in UiO-66-NH_2 This indicates a successful attachement of the CdS quantumdots to the MOF crystals. The CdS peak at 25.7° 2 θ can also be seen for UiO-66@CdS and UiO-66-NH_2@CdS and thereby confirming the CdS QD integration into the MOF structure.

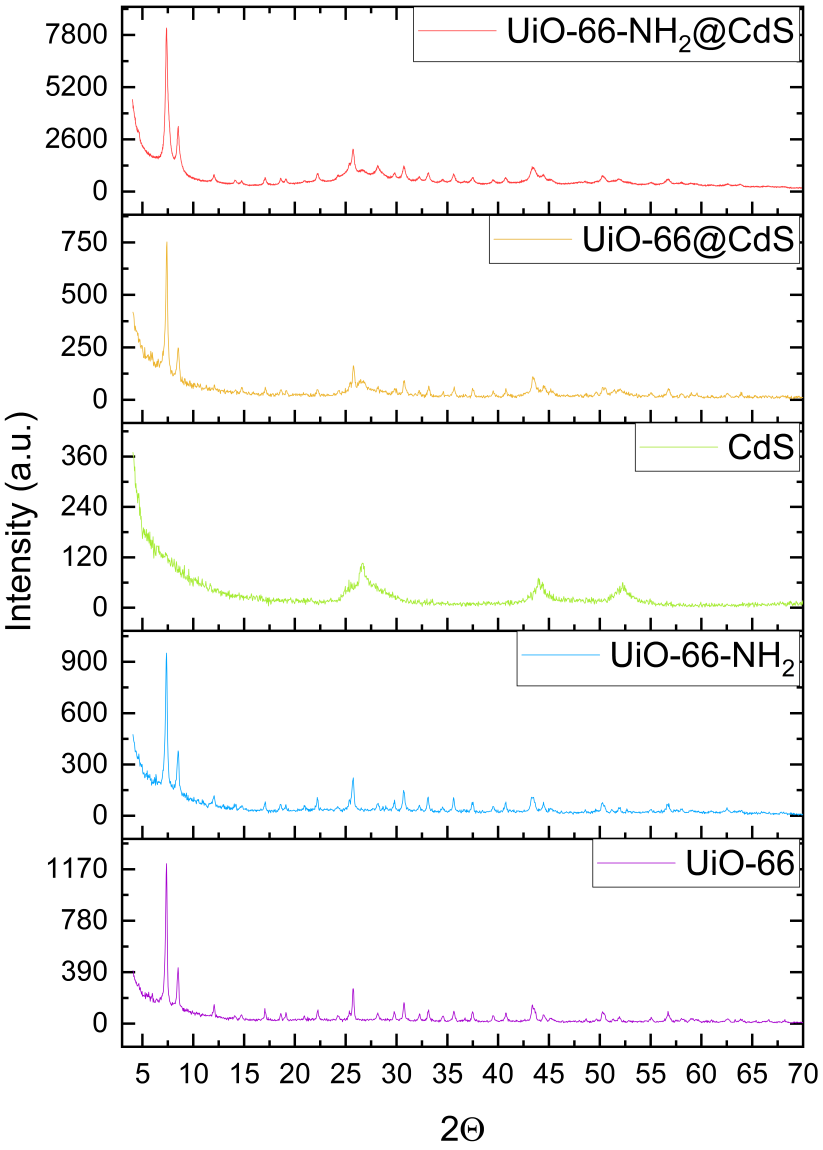


Figure 13: PXRD of synthesized MOF and CdS

3.1.1 BET measurements of MOFs

Table 7: BET results of MOFs

Sample	Pore volume (cm^3/g)	Surface area (m^2/g)	Fitting error (%)	Pore width (nm)
UiO-66-NH_2	0.497	1262.047	0.075	1.868
UiO-66-NH_2@CdS	0.423	1115.767	0.062	1.780

A clear change can be observed after the deposition of CdS onto the MOF.

3.1.2 TEM images of UiO-66-NH_2 and UiO-66-NH_2@CdS

TEM images were conducted by Lingcong Ge to observe UiO-66-NH_2 and the CdS QDs on the MOF structures and determine the shape and sizes. The goal of the synthesis was to achieve a nanocomposite of both materials and observe their catalytic activity upon irradiation. A qualitative look at the images can give broad but superficial insights into the quality of the synthesis. A first impression of the successful synthesis can be made but must be confirmed with other methods like PXRD as well.

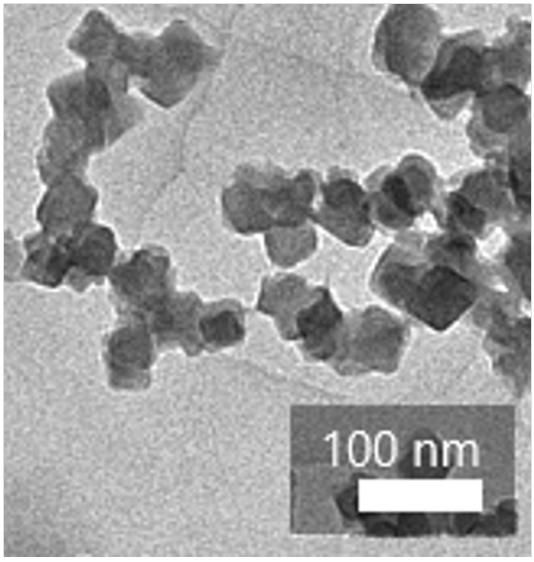


Figure 14: TEM of UiO-66-NH_2

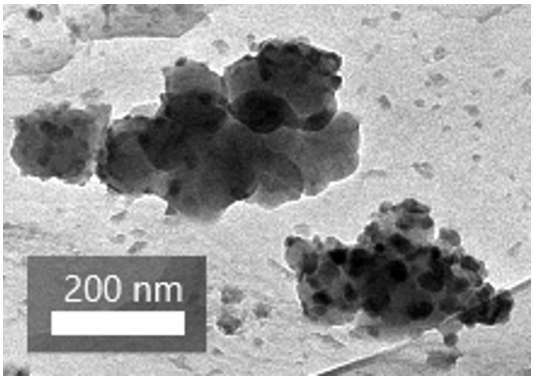


Figure 15: TEM of UiO-66-NH_2@CdS

In both figures the typical octahedral shape of UiO-66-NH_2 can be seen in different orientations.[60] Clear defects like intertwined growing or uneven crystals are observed. Th aim was to synthesise small MOFs to achieve a higher surface to bulk ratio. The contrast between the darker shaded CdS

QDs and the lighter shaded MOFs allows for a size determination of the QDs.

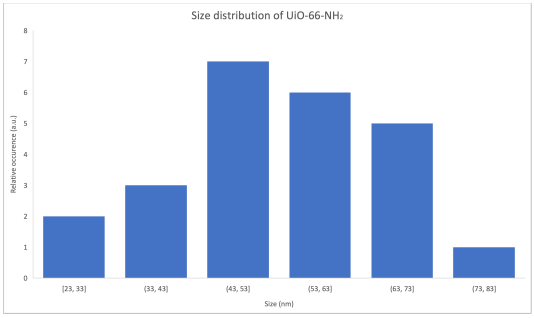


Figure 16: Size distribution of UiO-66-NH_2

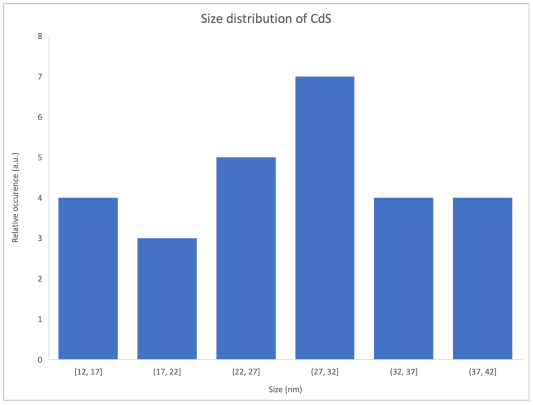


Figure 17: Size distribution of CdS

Th MOFs show a distribution from 23-83 nm. The CdS QDs show a broad distribution from 12-42 nm which is not in the desired range for QDs. The effect of the size is discussed at the next page.

3.1.3 Fabrication of UiO-66-NH_2-PVDF-HFP fiber

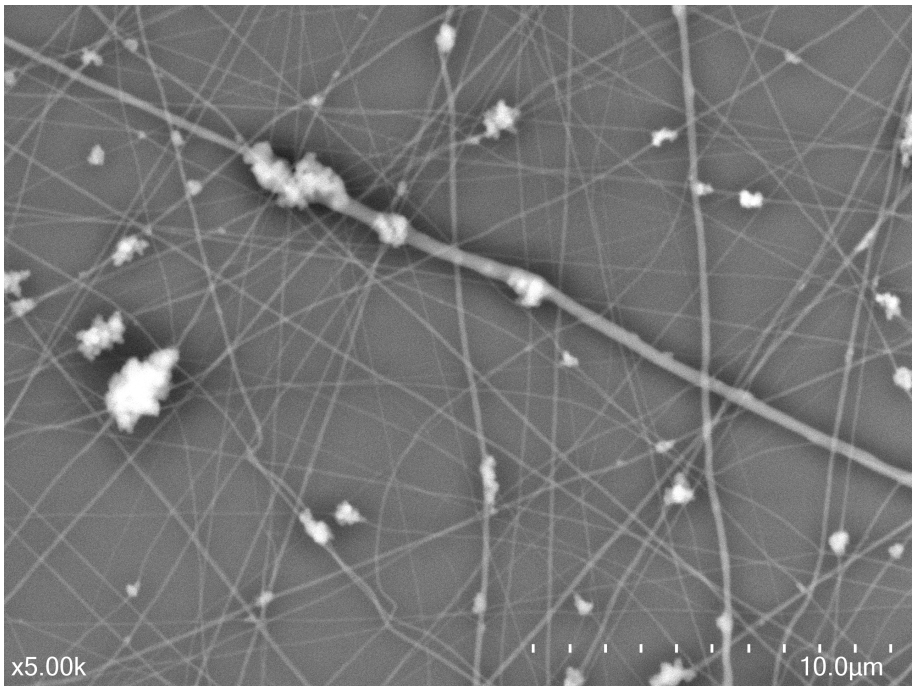


Figure 18: SEM image of UiO-66-NH_2-PVDF-HFP fiber

UiO-66-NH_2 was mixed into the polymer solution prior to electrospinning with the goal to incorporate the MOF crystals into the fibers. Ultra thin fibers incorporating UiO-66-NH_2 could be observed in SEM. Although slight accumulation of the MOF crystals can be seen an even distribution

3.1.4 CdS QDs

BET measurements show a pore size of the MOF seen in table 7 at 1.868 nm. Statistical analysis of the QDs which are seen in TEM shows an average size of 20-40 nm. That explains the lack of the desired optical properties because the synthesised particles exceed the size for it to show quantum mechanical behaviour.

Nevertheless, UiO-66-NH_2@CdS changes the pH in an aqueous solution upon irradiation of UV light with the wavelength of 365 nm which was monitored and discussed in a later part of this thesis.

3.1.5 Fluorescence spectroscopy

The sample was excited at wavelengths in the UV spectrum at 200-400 nm and the emission from wavelengths at 400-700 nm was measured.

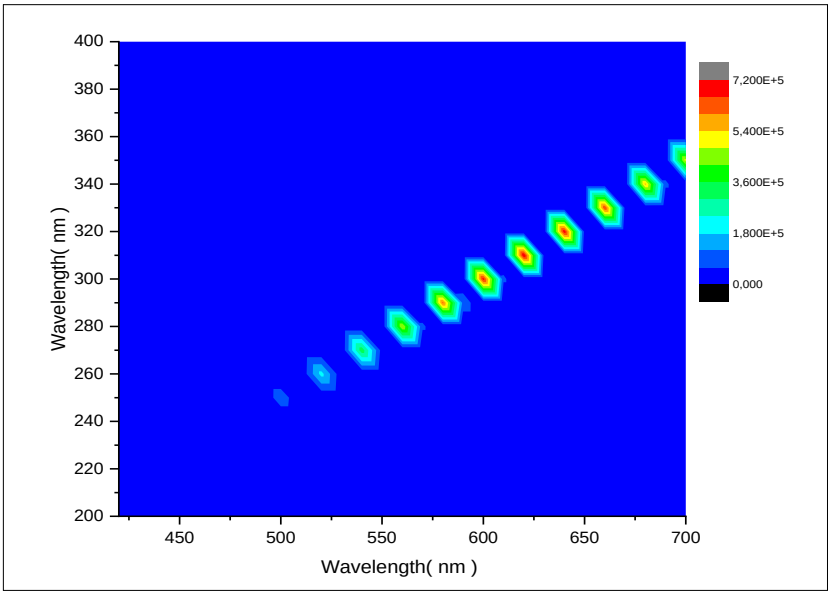


Figure 19: Fluorescence spectrum of UiO-66-NH_2

The emitted wavelength (λ) shows a direct relation to the excited wavelength. This pattern is observed for the measurements with UiO-66, UiO-66-NH_2; UiO-66@CdS and UiO-66-NH_2@CdS. The signals recorded do not show the pattern of fluorescence active substances of a sharp peak at a distinct wavelength. The peak of the signals is exactly 2λ which suggests rather constructive interference than actual fluorescence. Light moves in waves and those waves can interact with each other. Those interactions result in constructing interference when the phase difference of the wave is an even multiple of π. If the phase difference of the wave is an uneven multiple of π destructive

interference occurs.

That suggests that the measured samples show no flurorescence and only reflectance.[41] The samples are not optically activated by light with the wavelength from 200-400 nm.

3.1.6 Catalysis with TiO_2 powder

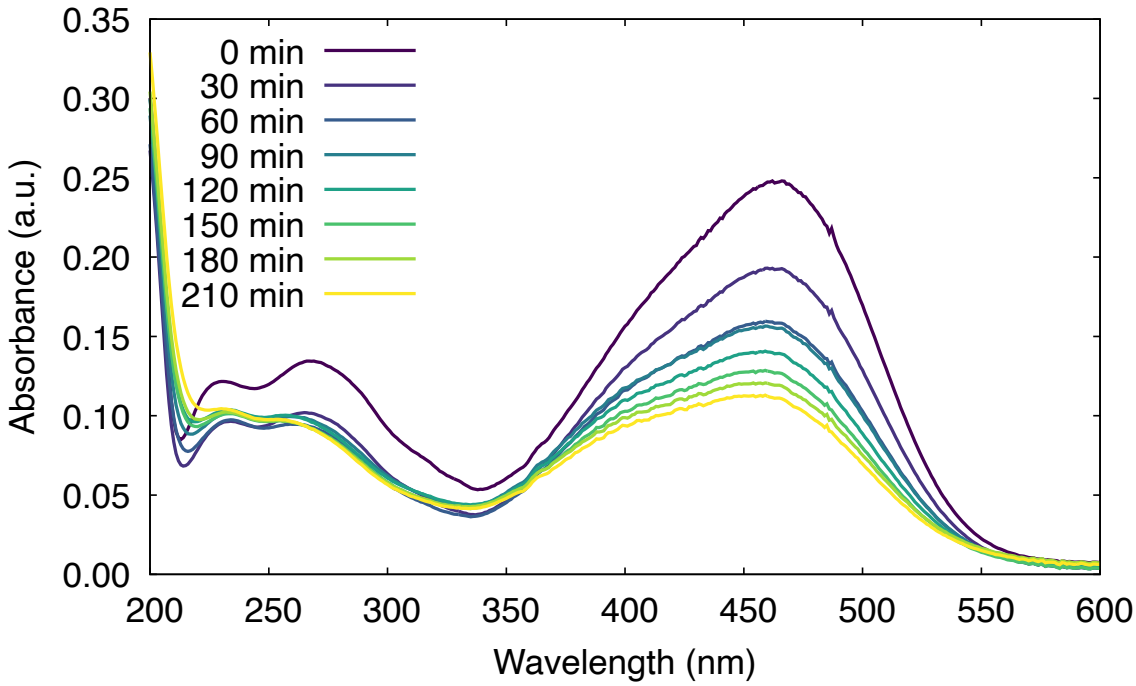


Figure 20: Photocatalysis of MO with TiO_2 powder

Degradation of the peak height at 424 nm can be observed over time. That indicates that the degradation of MO is aides by TiO_2 and UV light.

3.1.7 pH measurement

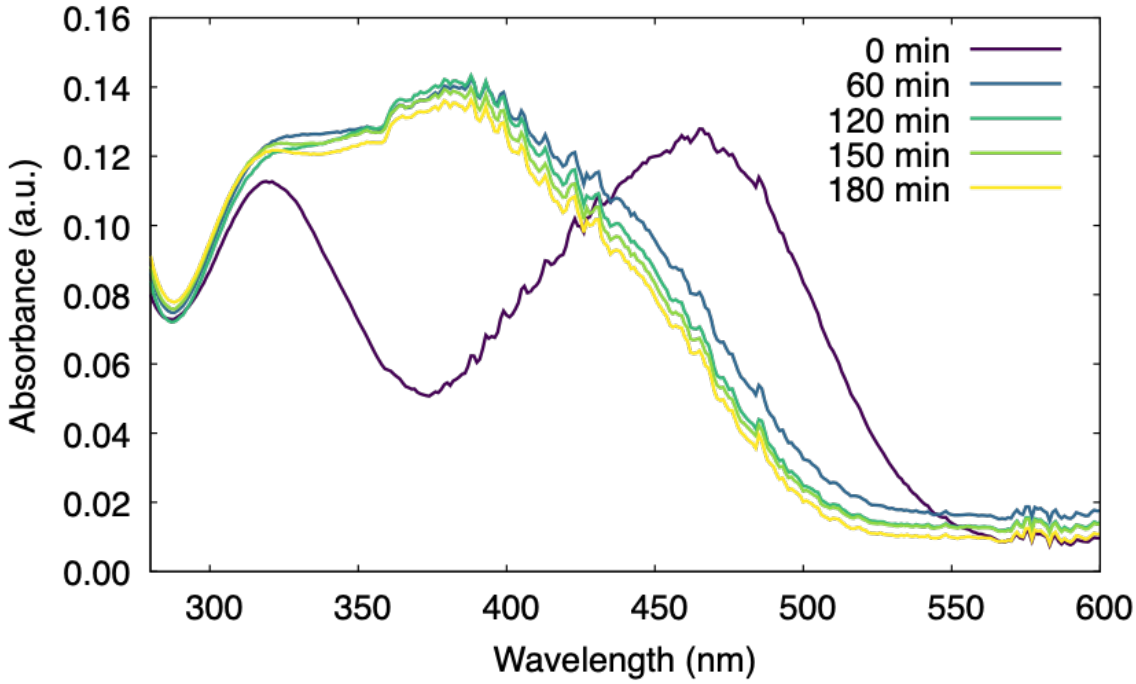


Figure 21: Peak shift of MO under UV radiation (365 nm, 100W) with UiO-66-NH_2@CdS

MO is a pH indicator with a protonated form in acidic environment and a deprotonated form in a basic environment. Both have a distinct absorption wavelength.[61]

In figure 21 one sees that the absorbance peak shifts towards lower wavelengths for longer irradiation times, indicating that a change in the pH value of the solution is occurring. To assure that hypothesis a direct pH measurement was conducted.

Table 8: Observed pH change during irradiation

Sample \ Wavelength	365 nm	400 nm
UiO-66	X	X
UiO-66-NH_2	X	X
UiO-66@CdS	X	X
UiO-66-NH_2@CdS	✓	X
CdS	X	X

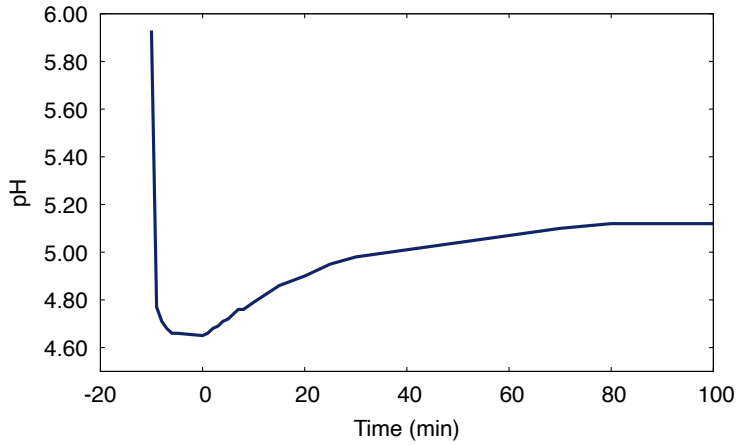


Figure 22: pH values of UiO-66-NH_2@CdS under UV radiation (365 nm, 100W)

The UV lamp (100 W, 365 nm) was switched on at 0 min and switched off at 90 min. A pronounced change in pH can be seen after switching on the lamp. After stopping UV irradiation the pH of the system does not recover.

This effect is only observed for UiO-66-NH_2@CdS at 365 nm and in no other combination. This might be caused by photocatalytic hole separation, as it is known that 'WP/UiO-66/CdS heterojunction' is able to convert protons into hydrogen. However in the reference literature[62] a 300 W xenon lamp with a cutoff filter of 420 nm was used. In this experiment a 50 W 365 nm lamp was used to investigate the photocatalytic effect.

With the assumption of the hydrogen concentration of the solution before and after irradiation according to the measured pH a total amount of around 35 μg of H_2 gas should be produced which is not measurable with the current instrumentation available in our lab. Further research is needed to grasp the effect in its full extent. The literature shows pH dependence of hydrogen evolution [63] and also pH change during hydrogen evolution is described.[64]

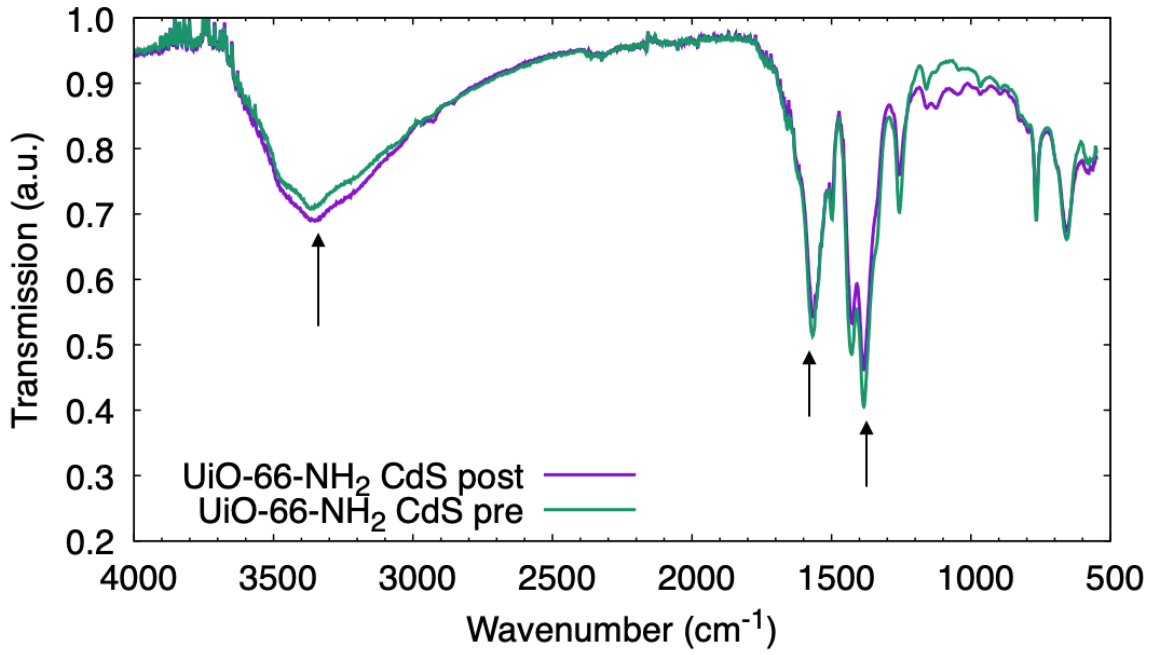


Figure 23: IR spectra of UiO-66-NH_2@CdS before and after catalysis

To confirm catalyst integrity after catalysis IR measurements were conducted. The O-H stretch mode at around 3450 cm^{-1} can be clearly indicated for the catalyst pre and post catalysis. The same applies to the N-H bend mode at around 1600 cm^{-1} and the C-N stretch mode at 1400 cm^{-1}. The N-H stretch mode at 3500-3300 cm^{-1} is overlayed by the broad strong O-H stretch mode and cannot be observed. The hypothesis of oxidation of the amino group to a nitro group can be discarded due to the fact that no N-O stretch mode at 1550-1500 cm^{-1} could be detected after the catalysis.

The following table shows the the functional groups which are detected in IR spectroscopy and their wavenumber.

Table 9: IR bands

Group	**Wavenumber** (cm^{-1})	**Mode**
O-H	3500-3000	stretch
C-N	1320	stretch
N-H	1620	bend
N-H	3500-3300	stretch
N-O	1550-1500	stretch

3.2 Fibermat synthesis

3.2.1 Fabrication of TiO_2 fiber

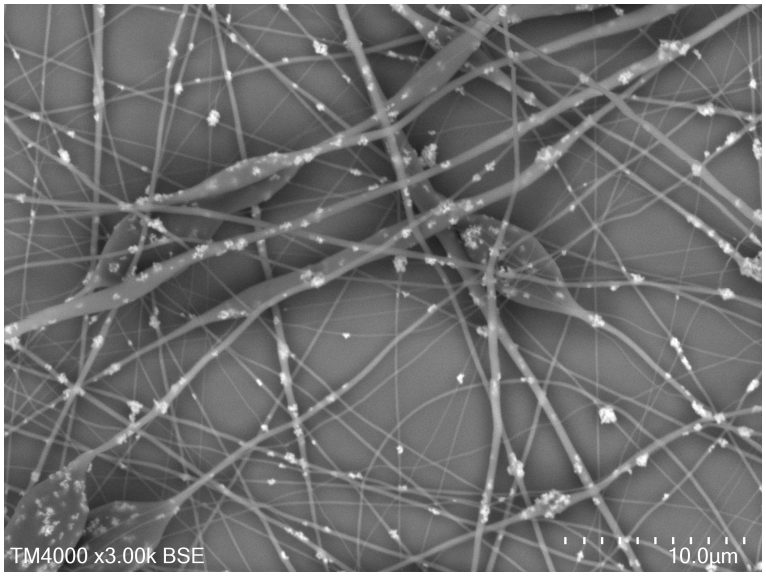


Figure 24: SEM image of TiO_2 PVDF-HFP fibermat

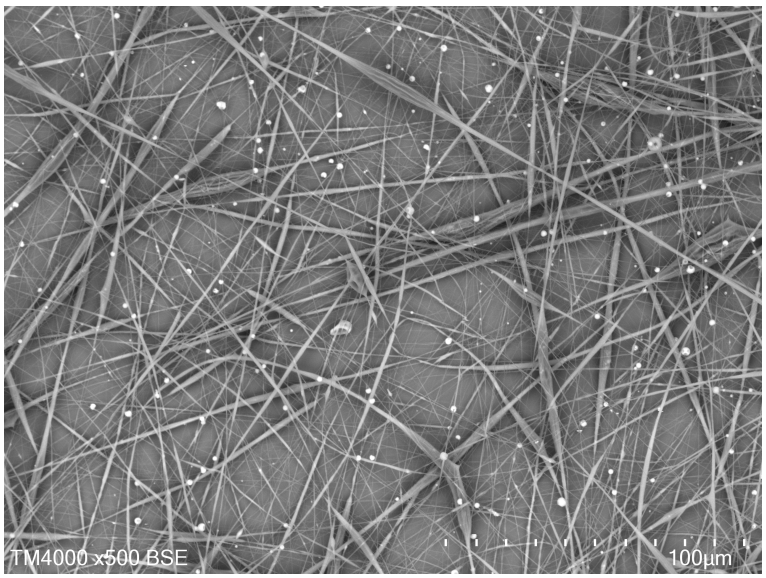


Figure 25: SEM image of $Ti(iOPr)_4$ PVDF-HFP fibermat

3.3 Growth of TiO_2 crystals on electrospun fibers

The $Ti(iOPr)_4$ containing fibermat showed after the hydrothermal reaction in the autoclave clear shrinking on a macroscopic scale and in the SEM image the fibers are distorted.



Figure 26: SEM image of TiO_2 crystals on fiber

crystals can be seen, and an elemental analysis was conducted via EDX to assure the composition of the crystals.

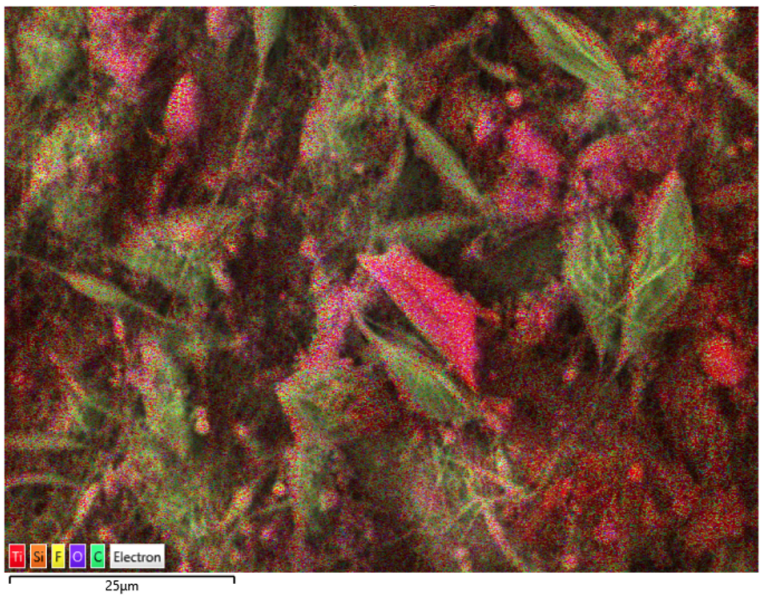


Figure 27: EDX image of TiO_2 crystals on fiber

EDX as a surface analytical method only shows the elemental composition of the compounds which lay on the surface and can be seen in the image. One can see the crystals which contain Ti here highlighted in red. Also, distorted fibers can be identified as containing carbon which is highlighted in green.

Table 10: Elemental composition of ADEL 29

Element	**wt%**	σ
C	27.3	0.3
Ti	26.0	0.1
F	22.2	0.2
O	21.6	0.3
Si	2.2	0.0
Ca	0.6	0.0

The elemental analysis confirms a high Ti content at the fiber.

3.4 Contact angle measurements

The following table shows the measured CAs of the prepared fibermats with the composition as listed below. The values are given below as measured where an X marks that no measuring of a CA was possible due to fast wetting of the fiber. Incubation of the fibers was conducted at ambient conditions in contact with air.

Table 11: CA measurement of fibermats. X indicates that no CA could be measured due to wetting of the surface

Sample	**Mean CA** (°)	**Standard deviation**
PVDF-HFP + TiO_2	129.96	1.56
PVDF-HFP + $Ti(iOPr)_4$	X	X
PVDF-HFP + $Ti(iOPr)_4$ after 2 weeks incubation	X	X
PVDF-HFP + TiO_2 after 2 weeks incubation	140.07	1.98
PVDF-HFP + $Ti(iOPr)_4$+ GNT	X	X
PVDF-HFP + $Ti(iOPr)_4$ + GO	141.19	2.29

As for some fibermats no CA could be measured due to the high wettability of the surface. The CA of ADEL 32 shows that the TiO_2 incorporated fibers show hydrophobic behaviour although TiO_2 in itself is hydrophilic.[65] This and the fact that the CA is similar to the CA of a plain PVDF-HFP fibermat (ADEL 26) leads to the conclusion that the TiO_2 in PVDF-HFP + TiO_2 fibermat does mi-

grate to the thermodynamically more favourable core during electrospinning and therefore is not photocatalyticly available.[66] The CA of ADEL 32 is slightly higher which can be explained due to increased surface roughness one sees in the CA measuring device.

3.4.1 TEM of Fibers with Ti(iOPr)$_4$

After incubation for two weeks at ambient conditions the Ti(iOPr)$_4$-PVDF-HFP fibers show wetting. To investigate the inner workings of the fiber composite a TEM was conducted. The transition metal Ti with its oxide and organometallic species can be distinguished in TEM via its darker shade. The polymer consisting of lighter compounds like hydrogen, fluorine and carbon show a light shading due to the lower electron density.[67] Also the material density has an influence in the shading of the TEM image.[68]

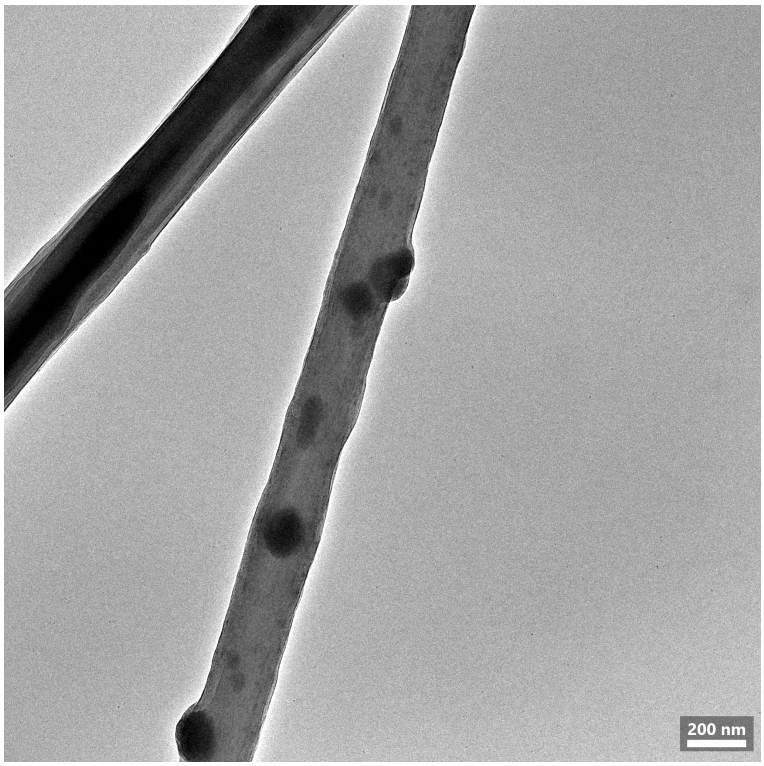


Figure 28: TEM image of Ti(iOPr)$_4$ fiber

In the figure above one sees the encapsulated organometal in the fibers. In one of both mapped fibers the one sees a core in a darker shade concluding that the Ti species lies embedded in the fiber.

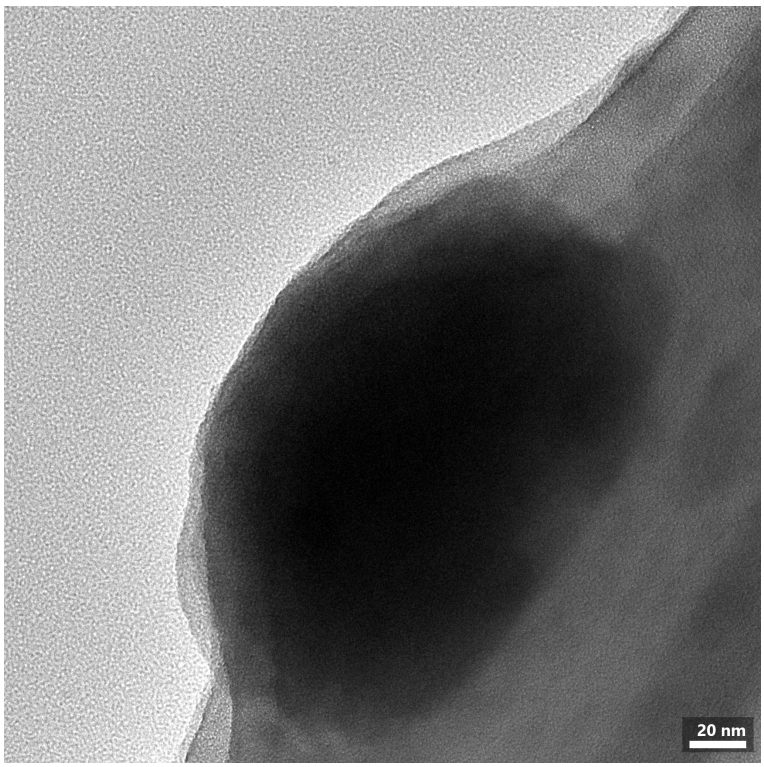


Figure 29: TEM image of Ti(iOPr)$_4$ fiber

The TEM image at a higher magnification shows an area of encapsulated Ti species. One can identify that the Ti species lies embedded into the fiber.

3.5 Crystal phases of PVDF-HFP

The alpha and beta phases show signals at distinct wavelengths. The intensities within a measurement are indicative of the relative concentrations and therefore a qualitative statement can be drawn.[60]

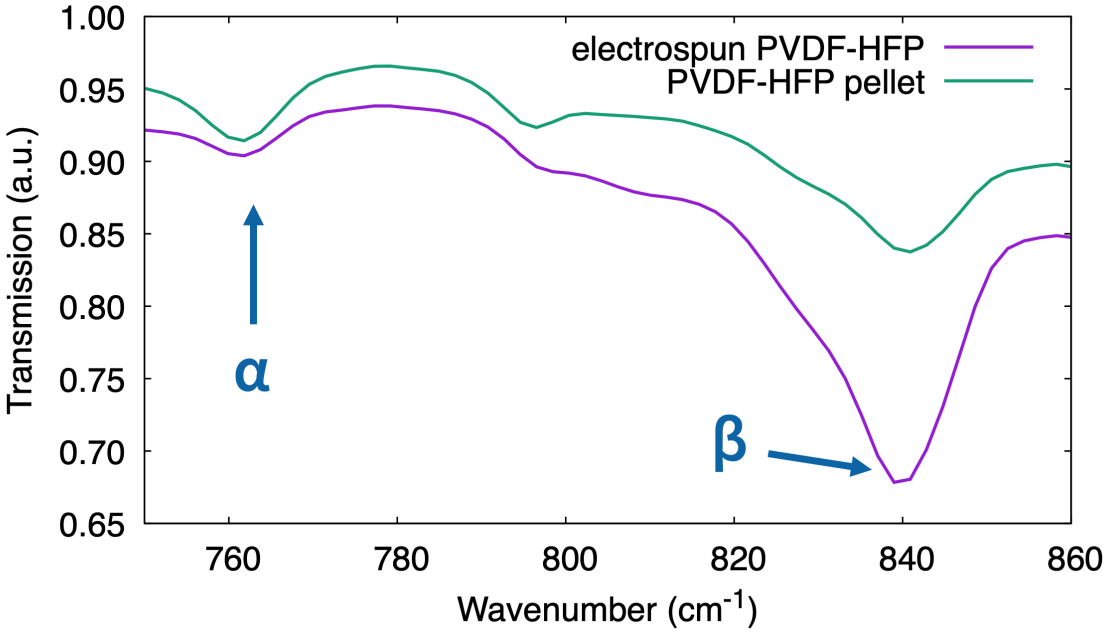


Figure 30: IR of PVDF-HFP

IR was chosen as a method to analyse the crystal phases of electrospun PVDF-HFP and the PVDF-HFP pellet. The alpha phase at 764 cm^{-1} and the beta phase at 840 cm^{-1} are highlighted with arrows. For the electrospun PVDF-HFP one sees an enhancement of the beta phase to alpha phase distribution in comparison to the PVDF-HFP pellet. [60]

3.6 Catalysis with fibermat

As an internal standard 1-Methylimidazole (1.5 μL) was added and the ratio of standard to MO was monitored. The 1-Methylimidazole peak at 197 nm was held as a reference at an absorbance at 1 as an internal standard. The peaks at 270 nm and 467 nm are assigned to MO. For the quantitative analysis a calibration with different concentrations of MO was conducted to compare the successful degradation processes in its efficiency.

3.6.1 Catalysis with Ti(iOPr)$_4$-PVDF-HFP fibermat

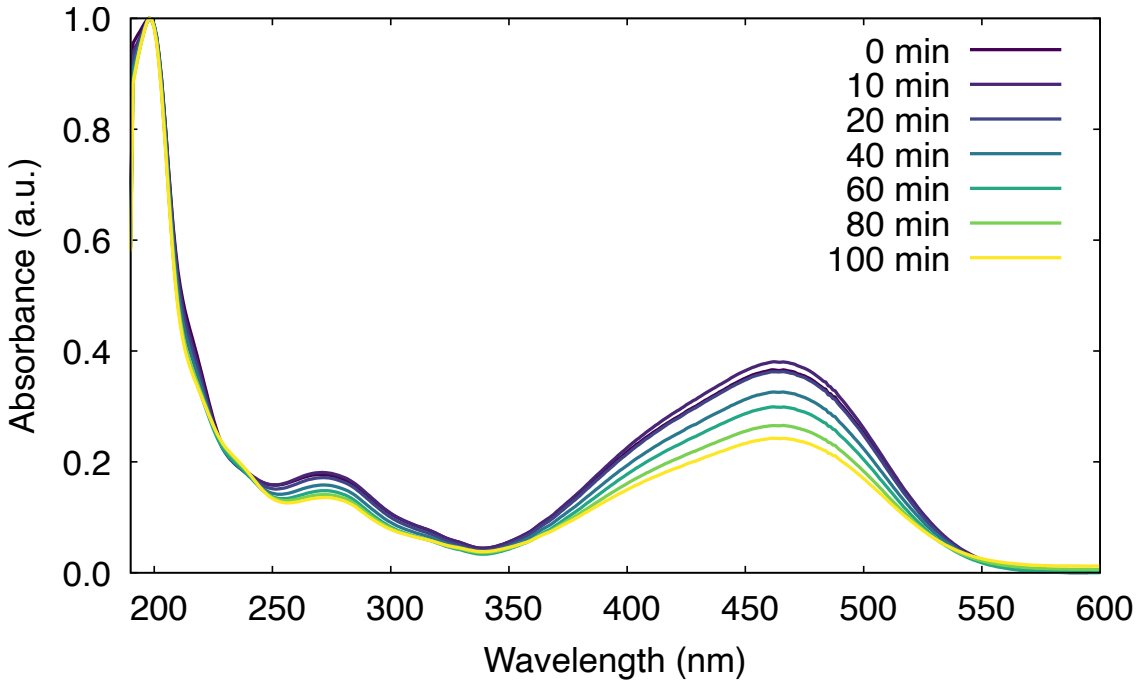


Figure 31: Catalysis with Ti(iOPr)$_4$-PVDF-HFP fibermat

A clear degradation over the time span of 100 min can be observed for the catalysis with Ti(iOPr)$_4$-PVDF-HFP fibermat. Both the peak at 270 nm and 467 nm are diminishing over time respective to the reference at 197 nm. The degradation seems to decelerate after 100 min.

3.6.2 Catalysis with Ti(iOPr)$_4$-PVDF-HFP-GNT fibermat

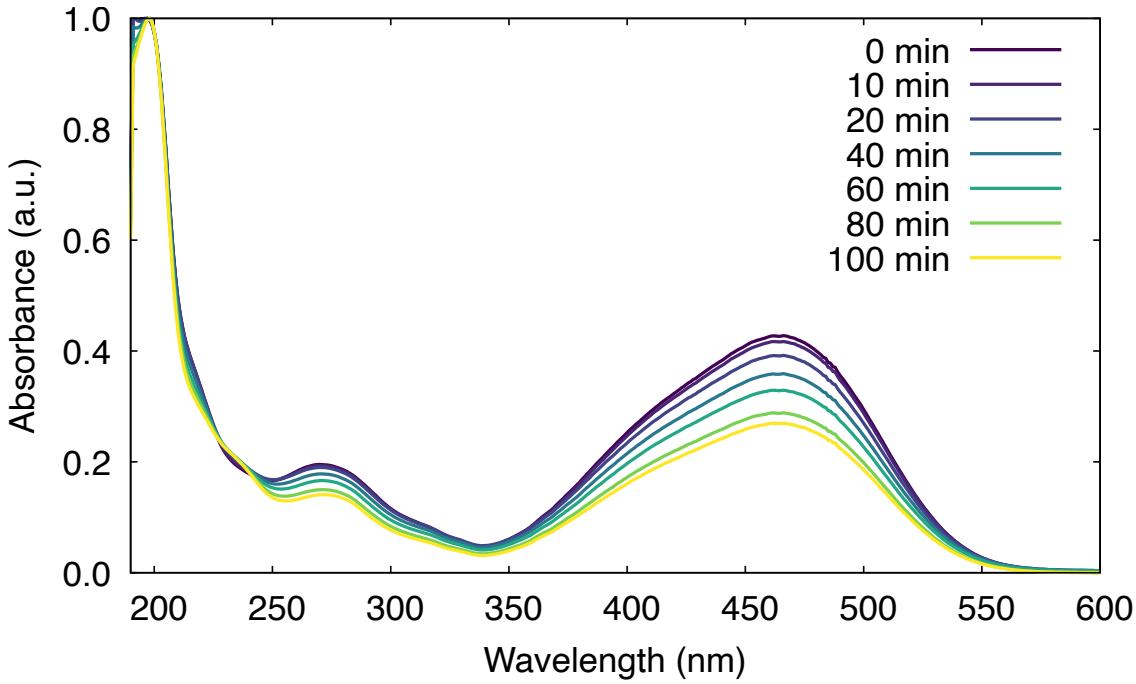


Figure 32: Catalysis with Ti(iOPr)$_4$-PVDF-HFP-GNT fibermat

A clear degradation over the time span of 100 min can be observed for the catalysis with Ti(iOPr)$_4$-PVDF-HFP fibermat. Both the peak at 270 nm and 467 nm are diminishing over time respective to the reference at 197 nm. The degradation seems to decelerate after 100 min.

3.6.3 Catalysis with Ti(iOPr)$_4$-PVDF-HFP-GO fibermat

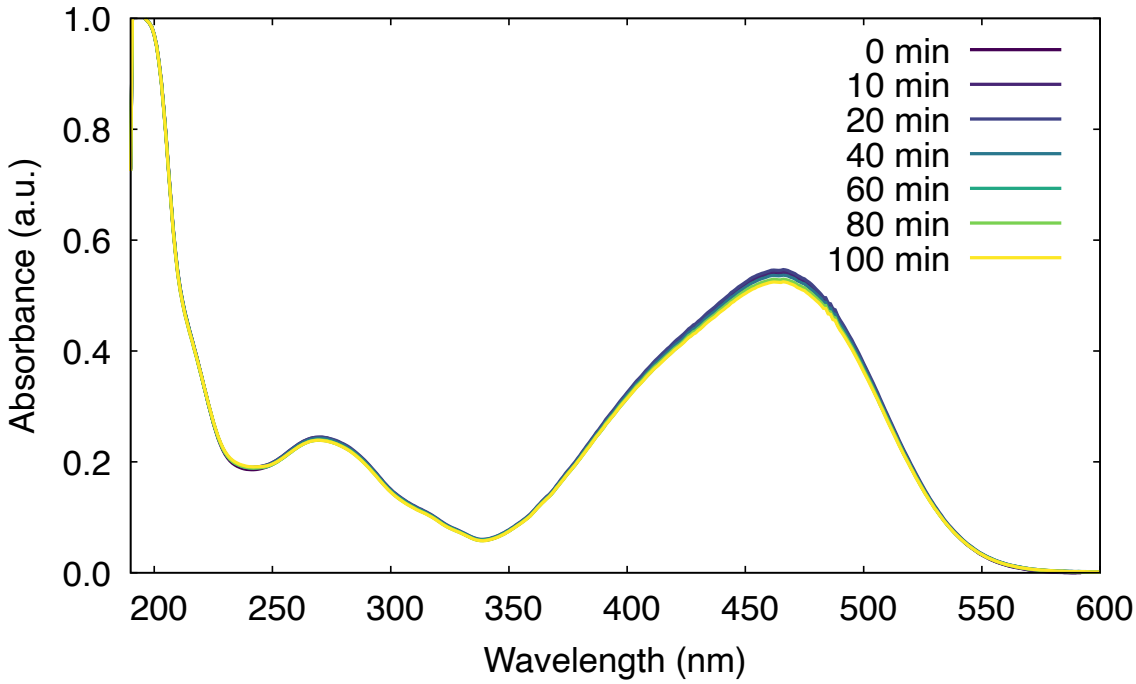


Figure 33: Catalysis with Ti(iOPr)$_4$-PVDF-HFP-GO fibermat

No degradation could be observed for the irradiation of the Ti(iOPr)$_4$-PVDF-HFP-GO fibermat over a time period of 100 min. The fibermat shows a high CA with water therefore hindering the accessibility of MO to the active Ti sites in the composite. MO as a polar chemical is dissolved in water. If the solvent cannot access the active sites due to hydrophobicity of the material the dye cannot be degraded.

3.6.4 Comparison of fibermat catalysis

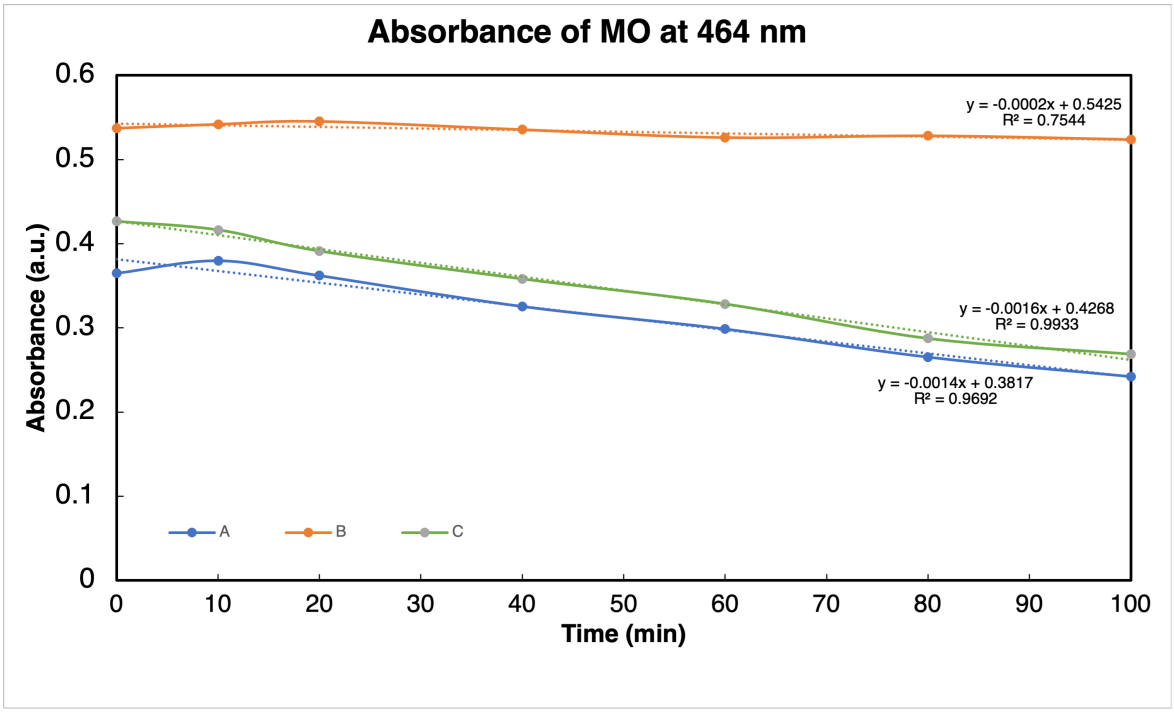


Figure 34: Degradation rate of MO during catalysis A: Ti(iOPr)4-PVDF-HFP fibermat B: Ti(iOPr)4-PVDF-HFP-GNT fibermat C: Ti(iOPr)4-PVDF-HFP-GO fibermat

Comparing the degradation rate of Ti(iOPr)4-PVDF-HFP fibermat and Ti(iOPr)4-PVDF-HFP-GNT fibermat show differences with the slope of -0.0014 and -0.0016 which is a derivation of 12.5 %. The degradation of Ti(iOPr)4-PVDF-HFP-GNT fibermat seems to occur faster. That could be due to the enhanced conductivity which was also reported previously.[60] Further statistical evaluation needs to be done to conclude and assure that effect.

4 Conclusion and outlook

The ideal procedure for electrospinning PVDF-HFP composites has been empirically determined for PVDF-HFP with a molecular weight of 400000 g/mol. Ideal conditions involved the preparation of the polymer solution at 40°C after overnight swelling and the use of an overhead stirrer to achieve a homogeneous solution for electrospinning. In order to incorporate solids into the solution to create an electrospinnable suspension, the mixtures were first sonicated, followed by magnetic stirring. That results in a stable solution which allows for further processing up to one week after preparation. Also a controlled argon atmosphere preparation of organic Ti^{4+} species to inhibit hydrolysis of the precursor has been established. The deposition of the composite fibermats on an aluminum covered collector plate and microscope glass slide was successfully conducted with further application. Through the discovery of PVDF-HFP $Ti(iOPr)_4$ fibers a novel method for presenting the Ti^{4+} species to the surface of the high surface energy polymer PVDF-HFP have been made accessible. The investigated process for fibermat preparation via electrospinning allows for high surface area fibermats. An increase in surface area drastically raises the probability of interaction in hetereogeneous catalysis applications. In conclusion the photocatalytic activity of TiO_2 has been linked with the mechanical durability of PVDF-HFP to achieve a novel composite.
Moreover, when GNT were additionally incorporated into the fibers the quantitative analysis shows a slight difference in catalytic activity. MO could be degraded via photo catalysis with $Ti(iOPr)_4$ incorporated PVDF-HFP fibers. The successful synthesis of co linked CdS/UiO-66 and CdS/UiO-66-NH_2 MOFs has been deducted. In a second approach UiO-66-NH_2, UiO-66@CdS and UiO-66-NH_2@CdS were incorporated into the PVDF-HFP fiber. Photocatalytic activity of UiO-66-NH_2@CdS has been observed and resulted in a pH change.

References

(1) Bafana, A.; Devi, S. S.; Chakrabarti, T. *Environmental Reviews* **2011**, *19*, 350–371.

(2) Huang, J. Y.; Li, S. H.; Ge, M. Z.; Wang, L. N.; Xing, T. L.; Chen, G. Q.; Liu, X. F.; Al-Deyab, S. S.; Zhang, K. Q.; Chen, T.; Lai, Y. K. *J. Mater. Chem. A* **2015**, *3*, 2825–2832.

(3) Boys, C. V. *Proceedings of the Physical Society of London* **1887**, *9*, 8–19.

(4) Gosline, J. M.; DeMont, M.; Denny, M. W. *Endeavour* **1986**, *10*, 37–43.

(5) Magoshi, J.; Magoshi, Y.; Nakamura, S. In *Silk Polymers*; Chapter 25, pp 292–310.

(6) Melelli, A.; Shah, D. U.; Hapsari, G.; Cortopassi, R.; Durand, S.; Arnould, O.; Placet, V.; Benazeth, D.; Beaugrand, J.; Jamme, F.; Bourmaud, A. *Nature Plants* **2021**, *7*, 1200–1206.

(7) Yang, C.; Jiang, X.; Gao, X.; Wang, H.; Li, L.; Hussain, N.; Xie, J.; Cheng, Z.; Li, Z.; Yan, J.; Zhong, M.; Zhao, L.; Wu, H. *Nano Letters* **2022**, *22*, PMID: 36054509, 7212–7219.

(8) Schweitzer, P. J.; Fallon, B. A.; Mann, J. J.; Kumar, J. D. *Drug Discovery Today* **2010**, *15*, 933–942.

(9) Cooley, J. F. *United Kingdom Patent* **1900**, *6385*, 19.

(10) Morton, W. J. Method of dispersing fluids. US Patent 705,691, 1902.

(11) Zhu, M.; Han, J.; Wang, F.; Shao, W.; Xiong, R.; Zhang, Q.; Pan, H.; Yang, Y.; Samal, S. K.; Zhang, F.; Huang, C. *Macromolecular Materials and Engineering* **2017**, *302*, 1600353.

(12) *Chemical Reviews* **2019**, *119*, 5298–5415.

(13) Radwan, A. B.; El-Hout, S. I.; Ibrahim, M. A. M.; Ismail, E. H.; Abdullah, A. M. *ACS Applied Polymer Materials* **2022**, *4*, 1358–1367.

(14) Gupta, P.; Elkins, C.; Long, T. E.; Wilkes, G. L. *Polymer* **2005**, *46*, 4799–4810.

(15) Reneker, D. H.; Yarin, A. L. *Polymer* **2008**, *49*, 2387–2425.

(16) Tang, W.; Fu, S.; Luo, N.; Fu, Q.; Chen, F. *ACS Applied Nano Materials* **2022**, *5*, 747–758.

(17) Chaudhary, K.; Kandasubramanian, B. *Industrial & Engineering Chemistry Research* **2022**, *61*, 3789–3816.

(18) Peterson, G. W.; Lee, D. T.; Barton, H. F.; Epps, T. H.; Parsons, G. N. *Nature Reviews Materials* **2021**, *6*, 605–621.

(19) Šutka, A.; Sherrell, P. C.; Shepelin, N. A.; Lapčinskis, L.; Mālnieks, K.; Ellis, A. V. *Advanced Materials* **2020**, *32*, 2002979.

(20) Sessler, G. M. *The Journal of the Acoustical Society of America* **1981**, *70*, 1596–1608.

(21) Gee, S.; Johnson, B.; Smith, A. *Journal of Membrane Science* **2018**, *563*, 804–812.

(22) Gregorio Jr., R. *Journal of Applied Polymer Science* **2006**, *100*, 3272–3279.

(23) Zhou, H.-C. "; Kitagawa, S. *Chem. Soc. Rev.* **2014**, *43*, 5415–5418.

(24) James, S. L. *Chem. Soc. Rev.* **2003**, *32*, 276–288.

(25) Freund, R.; Zaremba, O.; Arnauts, G.; Ameloot, R.; Skorupskii, G.; Dincă, M.; Bavykina, A.; Gascon, J.; Ejsmont, A.; Goscianska, J.; Kalmutzki, M.; Lächelt, U.; Ploetz, E.; Diercks, C. S.; Wuttke, S. *Angewandte Chemie International Edition* **2021**, *60*, 23975–24001.

(26) Ongari, D.; Talirz, L.; Smit, B. *ACS Central Science* **2020**, *6*, PMID: 33274268, 1890–1900.

(27) Zhevago, N. K.; Glebov, V. I. *Journal of Experimental and Theoretical Physics* **2017**, *124*, 845–853.

(28) Pitkänen, L.; Striegel, A. M. *TrAC Trends in Analytical Chemistry* **2016**, *80*, 311–320.

(29) Kumar, P.; Saxena, N.; Chandra, R.; Gupta, V.; Agarwal, A.; Kanjilal, D. *Nanoscale Research Letters* **2012**, *7*, 584.

(30) Xu, H.-Q.; Yang, S.; Ma, X.; Huang, J.; Jiang, H.-L. *ACS Catalysis* **2018**, *8*, 11615–11621.

(31) Wang, J.-L.; Wang, C.; Lin, W. *ACS Catalysis* **2012**, *2*, 2630–2640.

(32) Harrison, A.; Walton, M. *Solar Energy* **1978**, *20*, 185–188.

(33) Dudefoi, W.; Terrisse, H.; Popa, A. F.; Gautron, E.; Humbert, B.; Ropers, M.-H. *Food Additives Contaminants: Part A* **2018**, *35*, PMID: 29052468, 211–221.

(34) De Angelis, F.; Di Valentin, C.; Fantacci, S.; Vittadini, A.; Selloni, A. *Chemical Reviews* **2014**, *114*, PMID: 24926899, 9708–9753.

(35) Dong, D.; Li, P.; Li, X.; Zhao, Q.; Zhang, Y.; Jia, C.; Li, P. *Journal of Hazardous Materials* **2010**, *174*, 859–863.

(36) Guo, Q.; Zhou, C.; Ma, Z.; Ren, Z.; Fan, H.; Yang, X. *Chem. Soc. Rev.* **2016**, *45*, 3701–3730.

(37) Ma, Y.; Wang, X.; Jia, Y.; Chen, X.; Han, H.; Li, C. *Chemical Reviews* **2014**, *114*, PMID: 25098384, 9987–10043.

(38) Guo, Q.; Zhou, C.; Ma, Z.; Yang, X. *Advanced Materials* **2019**, *31*, 1901997.

(39) Guo, Q.; Zhou, C.; Ma, Z.; Ren, Z.; Fan, H.; Yang, X. *Annual Review of Physical Chemistry* **2018**, *69*, PMID: 29490209, 451–472.

(40) Peterson, J. J.; Krauss, T. D. *Nano Letters* **2006**, *6*, PMID: 16522053, 510–514.

(41) Samanta, A. *The Journal of Physical Chemistry B* **2006**, *110*, PMID: 16836314, 13704–13716.

(42) Amelino-Camelia, G.; Lämmerzahl, C.; Mercati, F.; Tino, G. M. *Phys. Rev. Lett.* **2009**, *103*, 171302.

(43) Kwok, D.; Neumann, A. *Advances in Colloid and Interface Science* **1999**, *81*, 167–249.

(44) Gao, L.; McCarthy, T. J. *Journal of the American Chemical Society* **2006**, *128*, PMID: 16834376, 9052–9053.

(45) Khawaji, A. D.; Kutubkhanah, I. K.; Wie, J.-M. *Desalination* **2008**, *221*, European Desalination Society and Center for Research and Technology Hellas (CERTH), Sani Resort 22 –25 April 2007, Halkidiki, Greece, 47–69.

(46) Pandey, S. *Kathmandu University medical journal (KUMJ)* **2006**, *4*, 128–134.

(47) Villeneuve, J.-P.; Banton, O.; Lafrance, P. *Ecological Modelling* **1990**, *51*, 47–58.

(48) Oller, I.; Malato, S.; Sánchez-Pérez, J. *Science of The Total Environment* **2011**, *409*, 4141–4166.

(49) Gogate, P. R.; Pandit, A. B. *Advances in Environmental Research* **2004**, *8*, 501–551.

(50) Imran, M.; Shaharoona, B.; Crowley, D. E.; Khalid, A.; Hussain, S.; Arshad, M. *Ecotoxicology and Environmental Safety* **2015**, *120*, 163–168.

(51) Chung, K.-T. *Journal of Environmental Science and Health, Part C* **2016**, *34*, PMID: 27635691, 233–261.

(52) Dirksen, A.; Zuidema, E.; Williams, R. M.; De Cola, L.; Kauffmann, C.; Vögtle, F.; Roque, A.; Pina, F. *Macromolecules* **2002**, *35*, 2743–2747.

(53) Katz, M. J.; Brown, Z. J.; Colón, Y. J.; Siu, P. W.; Scheidt, K. A.; Snurr, R. Q.; Hupp, J. T.; Farha, O. K. *Chem. Commun.* **2013**, *49*, 9449–9451.

(54) Shen, L.; Liang, S.; Wu, W.; Liang, R.; Wu, L. *J. Mater. Chem. A* **2013**, *1*, 11473–11482.

(55) Ke, F.; Wang, L.; Zhu, J. *Nano Research* **2015**, *8*, 1834–1846.

(56) Wang, X.; Xiao, C.; Liu, H.; Huang, Q.; Fu, H. *Journal of Applied Polymer Science* **2018**, *135*, 46711.

(57) Tan, J. Z. Y.; Nursam, N. M.; Xia, F.; Truong, Y. B.; Kyratzis, I. L.; Wang, X.; Caruso, R. A. *J. Mater. Chem. A* **2017**, *5*, 641–648.

(58) Kandiah, M.; Nilsen, M. H.; Usseglio, S.; Jakobsen, S.; Olsbye, U.; Tilset, M.; Larabi, C.; Quadrelli, E. A.; Bonino, F.; Lillerud, K. P. *Chemistry of Materials* **2010**, *22*, 6632–6640.

(59) Molavi, H.; Eskandari, A.; Shojaei, A.; Mousavi, S. A. *Microporous and Mesoporous Materials* **2018**, *257*, 193–201.

(60) Tong, W.; Zhang, Y.; Huang, H.; Xiao, K.; Yu, S.; Zhou, Y.; Liu, L.; Li, H.; Liu, L.; Huang, T.; Li, M.; Zhang, Q.; Du, R.; An, Q. *Nano Energy* **2018**, *53*, 513–523.

(61) Zaggout, F. R.; El-Ashgar, N. M.; Zourab, S. M.; El-Nahhal, I. M.; Motaweh, H. *Materials Letters* **2005**, *59*, 2928–2931.

(62) Zhang, Y.; Jin, Z. *Phys. Chem. Chem. Phys.* **2019**, *21*, 8326–8341.

(63) Lamoureux, P. S.; Singh, A. R.; Chan, K. *ACS Catalysis* **2019**, *9*, 6194–6201.

(64) Carneiro-Neto, E. B.; Lopes, M. C.; Pereira, E. C. *Journal of Electroanalytical Chemistry* **2016**, *765*, SI on Latin-American Researchers in ElectroChemistry, 92–99.

(65) Sakai, N.; Wang, R.; Fujishima, A.; Watanabe, T.; Hashimoto, K. *Langmuir* **1998**, *14*, 5918–5920.

(66) Lencar, C.; Ramakrishnan, S.; Erfanian, E.; Sundararaj, U. *Molecules* **2022**, *27*, 933.

(67) Kim, D.; Lee, J. S.; Barry, C. M.; Mead, J. L. *Microscopy Research and Technique* **2007**, *70*, 539–546.

(68) Gao, P.; Zhou, J.; Rong, W.; Gao, J.; Wang, L.; Sun, L. *Micron* **2021**, *141*, 102978.